

Detrital muscovite $^{40}\text{Ar}/^{39}\text{Ar}$ geochronology and provenance of Cenozoic deposits in the Qaidam basin, northern Tibetan Plateau and comparison with detrital zircon and apatite records

Shuhuai Ye^a, Xing Jian^{a,*}, Ling Fu^b, Wei Zhang^a, Xiaotian Shen^a, Ping Guan^c

^a State Key Laboratory of Marine Environmental Science, College of Ocean and Earth Sciences, Xiamen University, Xiamen 361102, PR China

^b Research Institute of Petroleum Exploration and Development (RIPED), PetroChina, Beijing 100083, PR China

^c MOE Key Laboratory of Orogenic Belts and Crustal Evolution, School of Earth and Space Sciences, Peking University, Beijing 100871, PR China

ARTICLE INFO

Keywords:

Qaidam basin

Provenance

Detrital muscovite $^{40}\text{Ar}/^{39}\text{Ar}$ records

Detrital zircon U-Pb records

Detrital apatite fission track records

ABSTRACT

The single-grain detrital multi-mineral dating techniques are powerful tools for tracing sediment provenance. However, natural biases in sediment source-to-sink systems may lead to heterogeneous sink signals based on detrital single-grain ages. Differing provenance interpretations may arise from detrital multi-mineral geochronologic data because of the potentially diverse origins and transport behaviors of the analyzed detrital minerals. To test this hypothesis, we present new single-grain detrital muscovite $^{40}\text{Ar}/^{39}\text{Ar}$ dating results from the Cenozoic Qaidam basin and compile published detrital muscovite $^{40}\text{Ar}/^{39}\text{Ar}$, detrital zircon U-Pb, and detrital apatite fission track age data to interpret muscovite provenance and to explore the potential inconsistencies among multi-dating results and related controlling mechanisms. Our results indicate that detrital muscovite grains from most Cenozoic deposits have a similar, dominated 300–400 Ma age range, with subordinate 200–300 Ma and 400–500 Ma. The new and compiled $^{40}\text{Ar}/^{39}\text{Ar}$ age data demonstrate that detrital muscovite records from the Cenozoic Qaidam basin are stratigraphically variable. Samples from middle fine-grained deposits-dominated strata, representing the paleo-megalake period, exhibit a relatively wider age range compared to those from lower and upper coarse-grained deposits-dominated strata, indicating a probable control of sedimentary environments. Comparisons of detrital muscovite, zircon, and apatite records indicate that the detrital zircon age spectra have the oldest ages, the widest age ranges, and the largest number of age groups. Detrital zircon and apatite age spectra exhibit higher spatial variations than detrital muscovite records, likely due to the distinct source-to-sink behaviors of these minerals. The magmatic, metamorphic, and uplift history of source terranes, along with system closure temperatures, originally determine detrital mineral age records, i.e., high-temperature systems yield older ages, and vice versa. Parent-rock types, mineral fertility, and weathering resistance control the numbers and probabilities of the detrital age clusters. Differences in mineral shape, density, and transport and depositional processes (i.e., different transport loads of light, platy minerals vs. heavy, granular minerals) may cause variations in age spectra. These differences in detrital mineral behaviors warrant more attention in multi-mineral dating-based sediment provenance studies. Additionally, $^{40}\text{Ar}/^{39}\text{Ar}$ age data compilation based on global Cenozoic sedimentary basins and modern rivers indicates that detrital muscovite records have potentials to determine tectonic settings, but climate-induced exhumation signals need to be distinguished before interpretation.

1. Introduction

Detrital single-grain dating (i.e., detrital geochronology and thermochronology) is a powerful tool for sediment provenance studies and is crucial for addressing various geoscience issues. These include tracing

sediment provenance and dispersal patterns, understanding sediment recycling (e.g., Andersen, 2005; Carrapa, 2010; Dickinson and Gehrels, 2008, 2009a, 2009b; Caracciolo et al., 2015; Moecher et al., 2019), assessing the timing of tectonic processes such as the onset and kinematic history of mountain building (e.g., Carrapa, 2010; DeCelles et al.,

* Corresponding author.

E-mail address: xjian@xmu.edu.cn (X. Jian).

<https://doi.org/10.1016/j.marpetgeo.2024.107068>

Received 4 June 2024; Received in revised form 17 August 2024; Accepted 20 August 2024

Available online 23 August 2024

0264-8172/© 2024 Elsevier Ltd. All rights are reserved, including those for text and data mining, AI training, and similar technologies.

2004; Gehrels, 2014; Najman et al., 1997; White et al., 2002), determining the maximum depositional age of otherwise undatable sedimentary units (e.g., Carrapa, 2010; Copeland, 2020; Dickinson and Gehrels, 2009b; Najman et al., 1997, 2001), evaluating source-sedimentary basin evolution (e.g., Carrapa, 2010; Fildani et al., 2009; Rahl et al., 2003), analyzing sediment lag-times and transfer rates (e.g., Najman et al., 2003, 2009, 2019; Stockli and Najman, 2020), and assessing post-depositional burial heating (e.g., Stockli and Najman, 2020). Unlike traditional petrography (e.g., Jian et al., 2013a; Critelli and Martín-Martín, 2022, 2024; Criniti et al., 2023), which focuses on sand or sandstone framework grain composition (Critelli et al., 2018, 2021, 2023; Critelli and Criniti, 2021), single-grain dating primarily targets accessory minerals (such as zircon, apatite, rutile, and muscovite) through radiometric isotopes or fission track analysis (Carrapa, 2010; Chew et al., 2020; von Eynatten and Dunkl, 2012).

Zircon is the most widely used accessory mineral for geochronological and thermochronological studies. Magmatic crystallization processes are commonly dated using zircon U-Pb isotopes, which have a high closure temperature of >900 °C (Carrapa, 2010; Cherniak and Watson, 2001; Dahl, 1997; Mezger and Krogstad, 1997). Cooling and exhumation processes are dated using zircon fission-track (ZFT) and (U-Th)/He (ZHe) techniques, with closure temperatures of around 210 ± 20 °C (Carrapa, 2010; Zaun and Wagner, 1985) and $171\text{--}196$ °C (average 183 °C; Reiners, 2005; Reiners et al., 2002, 2004), respectively. Zircon's high durability during sedimentary processes allows it to survive multiple sedimentary cycles (Garzanti, 2016; von Eynatten and Dunkl, 2012), making it an important and widely-used target for sedimentary provenance studies (e.g., Cawood and Nemchin, 2000; Dickinson and Gehrels, 2008, 2009a; Jian et al., 2020, 2024). Apatite is another common accessory mineral in magmatic, metamorphic, and clastic sedimentary rocks and is frequently used in low-temperature thermochronology studies (e.g., Chew et al., 2020; Jian et al., 2018; Mark et al., 2016; von Eynatten and Dunkl, 2012; Wang et al., 2022a; Wang et al., 2017). Similar to zircon, apatite U-Pb, fission track (FT), and (U-Th)/He (AHe) techniques elucidate cooling and exhumation processes with closure temperatures of ca. $400\text{--}500$ °C (Chamberlain and Bowring, 2001), ca. $60\text{--}120$ °C (Green et al., 1989), and ca. $60\text{--}80$ °C (Carrapa et al., 2009; Farley, 2000), respectively. Multiple dating, i.e., U-Pb, FT, and (U-Th)/He dating on the same crystals (both zircon and apatite), has a high potential to reveal the entire cooling history of rock from crystallization to near-surface exhumation (Carrapa, 2010; Danišik et al., 2010). However, these techniques do not resolve mid-temperature (ca. $300\text{--}400$ °C) geological processes. The $^{40}\text{Ar}/^{39}\text{Ar}$ dating of K-bearing minerals (such as muscovite, biotite, amphibole, and feldspar) may fill this gap and muscovite is the most commonly used K-bearing mineral (Hodges et al., 2005; Stuart, 2002). With the Ar isotope closure temperature of ca. $350\text{--}400$ °C (Stuart, 2002), muscovite $^{40}\text{Ar}/^{39}\text{Ar}$ ages document the time when a rock mass passed through 8–10 km beneath actively eroding mountain belts (Hames and Bowring, 1994; Stuart, 2002).

Natural environmental bias (e.g., various parent rocks and sedimentary environments) may cause detrital single-grain ages to indicate different sources (Malusà and Garzanti, 2019; Chew et al., 2020; Criniti et al., 2024). Studies based on different detrital minerals (such as heavy and light minerals with different shapes) may provide dissimilar provenance interpretations due to various origins and different transport-depositional behaviors (Chew et al., 2020; Malusà et al., 2013, 2016; Malusà and Garzanti, 2019). Although combining geochronologic data from several detrital mineral species (multi-dating) is beneficial to better understand sedimentary provenance and basin-range evolution (e.g., Carrapa et al., 2009; Danišik et al., 2010; Kirkland et al., 2020; Xu et al., 2017), how to treat different provenance interpretations, if any, is usually a troublesome issue. To discuss the potential biases of single-grain dating and inconsistencies among multi-dating results, and to explore the underlying mechanisms, we focus on detrital muscovite, zircon, and apatite records from the Cenozoic Qaidam basin in the

northern Tibetan Plateau (Fig. 1). The Qaidam basin contains an unusually thick (3–16 km) Cenozoic sedimentary sequence, i.e., 3 km for margin and 16 km for the center (the center is in the western part of the basin). These Cenozoic deposits are thought to be mainly derived from the surrounding mountain ranges (Cheng et al., 2015, 2016, 2019a, 2019b, 2021; Jian et al., 2013a, 2013b, 2018, 2024; Lu et al., 2018, 2022b; Rieser et al., 2006b; Wu et al., 2012b) Wu et al., 2012a. The Qilian, Altun, and Eastern Kunlun Mountains are considered as the source areas for the Cenozoic Qaidam basin and contain kinds of metamorphic sedimentary rocks, especially the Qilian Mountains, (Gehrels et al., 2003a, 2003b; Rieser et al., 2005; Jian et al., 2013a, 2018, 2024; Cheng et al., 2015, 2016; Fu et al., 2022; Wang et al., 2023) which may have high muscovite fertility. Previous studies have shown relatively high detrital muscovite contents in some Cenozoic Qaidam basin sandstones (Fig. 2; Jian et al., 2013a; Rieser et al., 2005, 2006a, 2006b). Numerous detrital zircon and apatite age data from the Cenozoic deposits have been published (e.g., Cheng et al., 2019a; He et al., 2020, 2021a, 2021b; Jian et al., 2018, 2024 and reference therein; Wang et al., 2017, 2022a). These conditions make the Cenozoic Qaidam basin an ideal place to discuss the source-to-sink behaviors and mechanisms of detrital muscovite, zircon, and apatite grains and to verify potential dissimilar provenance interpretations based on single-grain dating results.

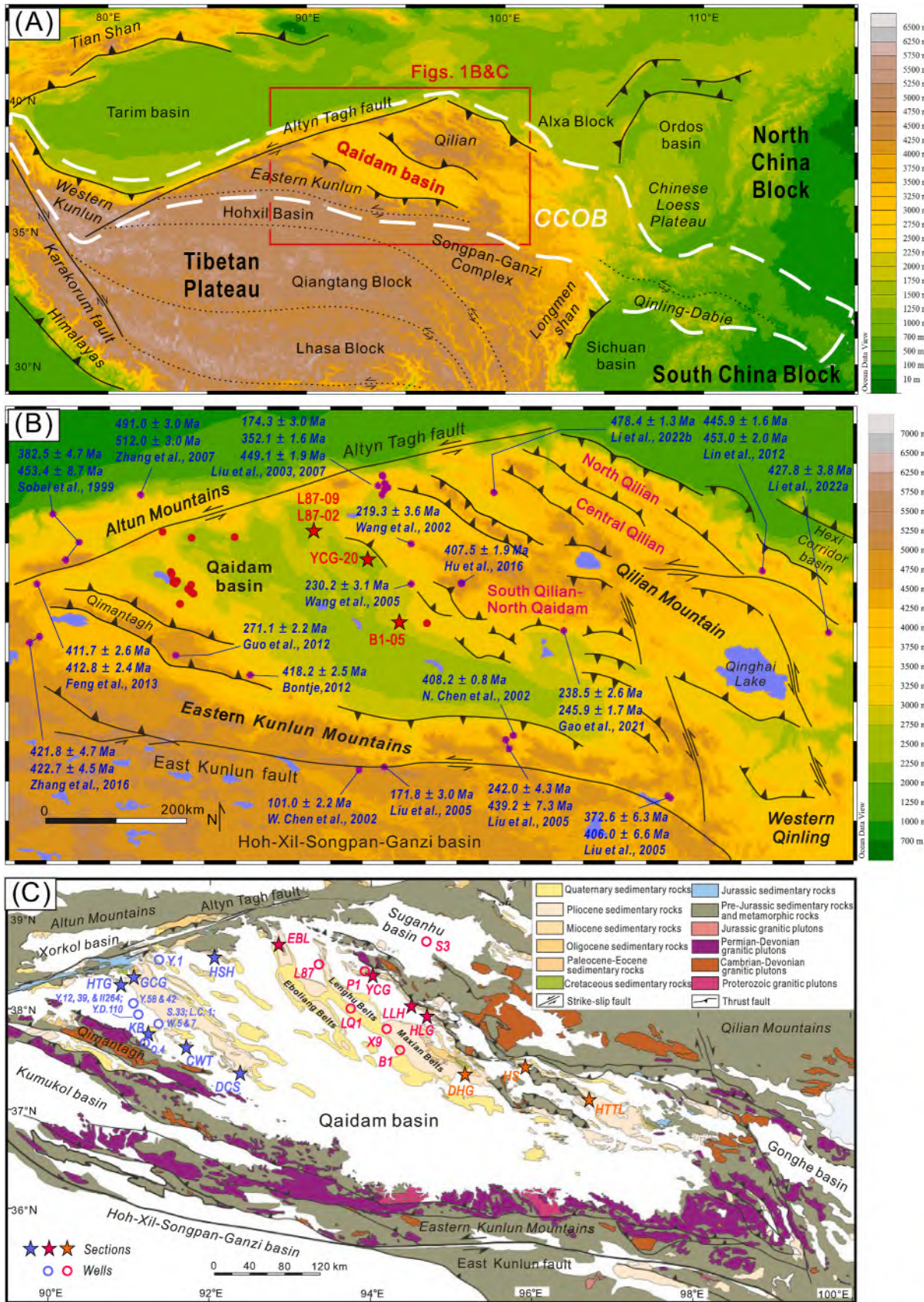
In this study, we present new sandstone (involving borehole and outcrop samples) detrital muscovite $^{40}\text{Ar}/^{39}\text{Ar}$ dating data ($n = 194$) from the northern Qaidam basin. We also compile published detrital muscovite $^{40}\text{Ar}/^{39}\text{Ar}$ ages from other regions of the Qaidam basin ($n = 520$), other Cenozoic sedimentary basins ($n = 5583$), and modern river basins ($n = 8058$) worldwide. Published detrital zircon U-Pb age data ($n = 12978$) and detrital apatite fission track (AFT) data ($n = 3364$) from the Cenozoic Qaidam basin are also compiled in this contribution. All the involved dating data are shown in the supplemental materials (Tables S1–S9 in Appendix A). The aims are to: 1) clarify the spatial and stratigraphic distributions of the Qaidam basin detrital muscovite $^{40}\text{Ar}/^{39}\text{Ar}$ age records, and explore related controlling mechanisms; 2) investigate detrital muscovite, zircon, and apatite age responses to their potentially different source-to-sink behaviors, and discuss the role of detrital muscovite in provenance analysis; 3) analyze the relationship between tectonic setting and detrital muscovite $^{40}\text{Ar}/^{39}\text{Ar}$ age spectra on a global scale.

2. Geological setting

2.1. The Qaidam basin and the surrounding mountain ranges

The Qaidam basin covers ca. $120,000$ km² and is situated at an elevation of ca. 2.7–3.0 km above sea level (Fig. 1B). It is bounded by the Qilian Mountains to the northeast, the Altun Mountains to the northwest, and the Eastern Kunlun Mountains to the south. These mountain ranges are significant components of the Central China Orogenic Belt (CCOB; Fig. 1A; Dong et al., 2021).

The Qilian Mountains are mainly composed of various types of metamorphic rocks, volcanic rocks, marine sedimentary strata, and ophiolite associations (Fig. 1C; Dong et al., 2021; Fu et al., 2022; Jian et al., 2013a; Rieser et al., 2005; Wang et al., 2023). The Qilian orogen is thought to have formed through the breakup of the supercontinent Rodinia, followed by subduction and collision involving the Alxa-North China, Central Qilian, and Qaidam Blocks during the Neoproterozoic to late Paleozoic ($>ca.$ 550–415 Ma; Dong et al., 2021; Jian et al., 2018, 2024; Li et al., 2020). These blocks experienced a magmatic lull from the late Paleozoic to the Triassic and underwent extension from the Jurassic to the Cretaceous likely due to the Lhasa-Qiangtang collision (Chen et al., 2021; Li et al., 2020; Lin et al., 2019; Tong et al., 2020; Zuza et al., 2018). The early Cenozoic witnessed the reactivation of the Qilian orogen, influenced by the far-field effect of the India-Asian collision (Chen et al., 2021; Li et al., 2020; Lin et al., 2019; Tong et al., 2020; Zuza



(caption on next page)

Fig. 1. (A) Topographic map of the Tibetan Plateau and its surrounding regions with their geological background. The white dashed lines mark the area of the Central China Orogenic Belt (CCOB). (B) Topographic map of the northeastern Tibetan Plateau showing the locations of the Qaidam basin, surrounding mountain ranges, and tectonic units. The red stars show the detrital muscovite $^{40}\text{Ar}/^{39}\text{Ar}$ dating sample locations in this study. The dots in red color show the locations of detrital muscovite $^{40}\text{Ar}/^{39}\text{Ar}$ dating samples from previous studies in the Cenozoic deposits. The purple dots show the locations of muscovite $^{40}\text{Ar}/^{39}\text{Ar}$ dating samples from previous studies in surrounding mountain ranges. Previous detrital muscovite $^{40}\text{Ar}/^{39}\text{Ar}$ geochronologic data are from Rieser et al. (2006a, 2006b, 2007, 2010) and the previous muscovite $^{40}\text{Ar}/^{39}\text{Ar}$ geochronologic data are from Bontje (2015); N. Chen et al. (2002); W. Chen et al. (2017); Fang et al. (2018); Hu et al. (2016); H. Li et al. (2022); Y. Li et al. (2022); Liu et al. (2007); Liu et al. (2003); Liu et al. (2005); Sobel and Arnaud (1999); Tian et al. (2020); Wang et al. (2002); Wang et al. (2005); Xu et al. (2002); Zhang et al. (2007); Feng et al. (2013); Guo et al. (2012); Lin and Zhang (2012); Zheng et al. (2016); Gao et al. (2021). (C) Geologic map of the Qaidam basin and its surrounding mountain ranges modified from Lu et al. (2018) with drilling wells (circles) and outcrop sections (stars) mentioned in this paper. HTTL: Huaitoutala section; HS: Hongshan section; DHG: Dahonggou section; B1: well B1, Beilingqiu region; X9: well X9; HLG: Hongliugou section; LLH: Lulehe section; YCG: Yingchaogou section; P1: well P1, Pingtai region; SGH: well SGH, Suganhu region; L87: well L87; LQ1: well LQ1; EBL: Eboliang section; HSH: Hongsanhan section; GCG: Ganchaigou section; HTG: Huatugou section; KB: Kunbei section; CWT: Changweitai section; DCS: Dongchaishan section; Y.1: well Yue1; Y.12, 39, & II264: wells Yue12, Yue39, and YueII264; Y.D.110: well Yuedong110; Y.58 & 42: wells Yue58 and Yue 42; S.3: Sha33; W.5 & 7: wells Wu5 and Wu7; Q.4: well Qie4.

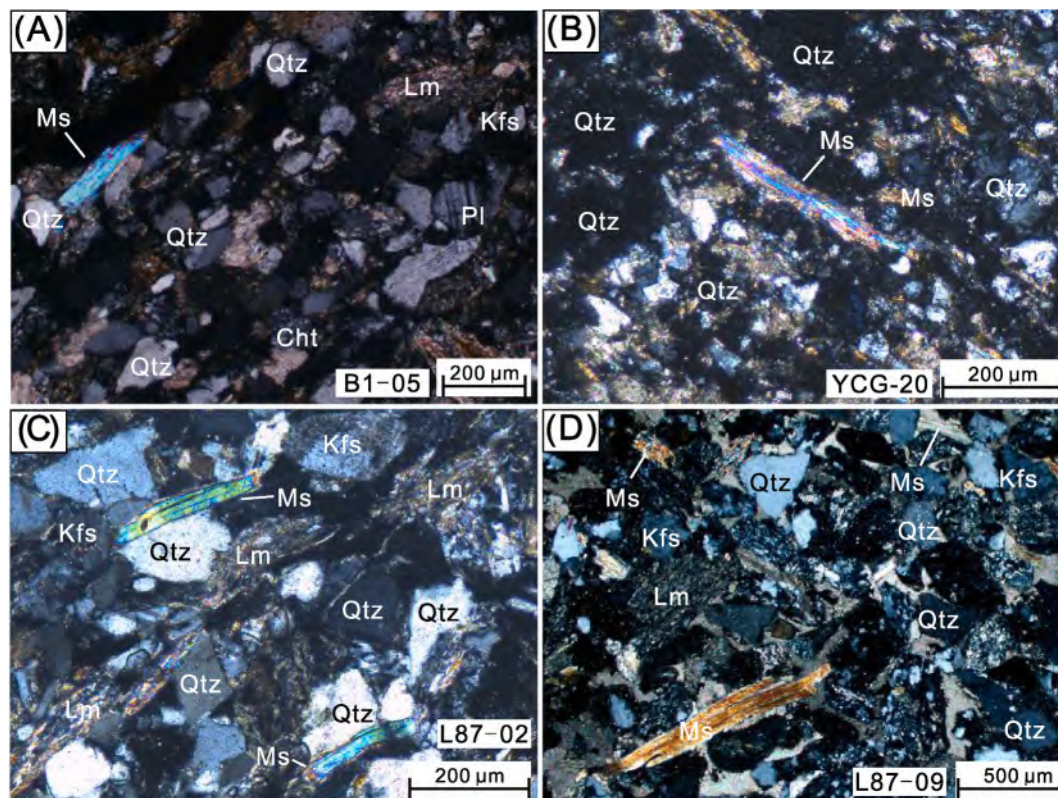


Fig. 2. Photomicrographs of sample B1-05 (A), sample YCG-20 (B), sample L87-02 (C), and sample L87-09 (D). Notice the high concentration of detrital muscovite. Photomicrographs modify from Jian et al. (2013a). Qtz: quartz; Kfs: K-feldspar; Pl: plagioclase; Ms: muscovite; Lm: metamorphic lithic; Cht: Chert.

et al., 2018; Li et al., 2022).

The Altun Mountains are renowned for their ultra-high pressure (UHP) metamorphism and the Mesozoic–Cenozoic sinistral strike-slip tectonic settings (Dong et al., 2021, Fig. 1B). This orogen consists mainly of Archean-Proterozoic basement rocks and marine sedimentary strata, Paleozoic metamorphic and magmatic rocks, and Mesozoic sedimentary strata (Fig. 1C; Allen et al., 2023; Dong et al., 2021; Gehrels et al., 2003a; Jian et al., 2018). It shares a similar Paleozoic tectonic history with the Qilian Orogen (>ca. 520–385 Ma; Dong et al., 2021; Sobel and Arnaud, 1999; Sobel et al., 2001). Multi-stage displacements of the Altyn-Tagh fault from the Mesozoic to the Cenozoic resulted in several cooling and exhumation events in the Altun Mountains (Dong et al., 2021; Shi et al., 2018; Sobel et al., 2001; Wu et al., 2012b).

The Eastern Kunlun Mountains are geographically separated from the Kunlun Orogen by the Altyn-Tagh fault (Fig. 1A). This orogen is mainly composed of Early Cambrian to Early Devonian and Late Permian to Triassic magmatic rocks, Devonian to Early Triassic marine sedimentary rocks, and Jurassic and Cenozoic non-marine rocks (Allen

et al., 2023; Dai et al., 2013; Dong et al., 2021; Jian et al., 2018). The Eastern Kunlun Mountains record a prolonged history of subduction and accretion related to the Proto-Tethys and Paleo-Tethys oceans during the Paleozoic to early Mesozoic (>485–220 Ma; Dong et al., 2021; Jian et al., 2024; Jian et al., 2018; Wang et al., 2023). Exhumation events in the Eastern Kunlun regions are regarded to be associated with the Qiangtang-Kunlun collision in the Early Jurassic, the Lhasa-Qiangtang collision from the Late Jurassic to Cretaceous, and the India-Asia collision since the early Cenozoic (Dai et al., 2013; Staisch et al., 2020; Tian et al., 2020; Wang et al., 2018; Wu et al., 2019a; Yuan et al., 2006).

2.2. Cenozoic stratigraphy, lithology, and sedimentary environments

The Cenozoic succession in the Qaidam basin is regularly divided into seven stratigraphic units: 1) Lulehe Formation (E_{1+2}), 2) Xiangan-chaiogou Formation (E_3), 3) Shanggan-chaiogou Formation (N_1), 4) Xiayoushshan Formation (N_2^1), 5) Shangyoushshan Formation (N_2^2), 6) Shizigou Formation (N_2^3), and 7) Qigequan Formation (Q_{1+2}) (Fig. 3; Ji

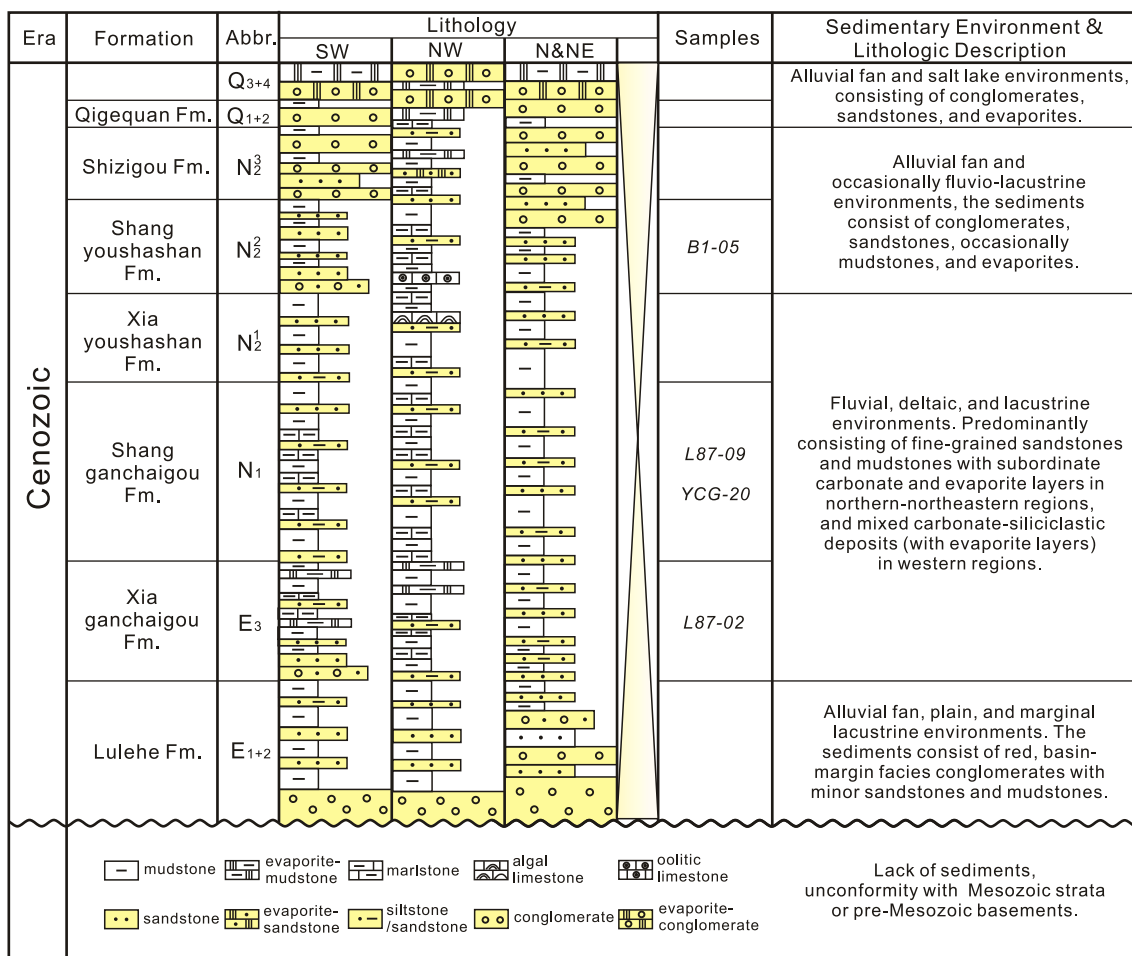


Fig. 3. Cenozoic stratigraphic framework, sedimentary environment, and lithological description of the Qaidam basin in northern Tibet, modified from Wang et al. (2023).

et al., 2017; Xing et al., 2023). There is ongoing debate about the depositional ages of these Cenozoic strata (Cheng et al., 2019a, 2019b, 2021; Jian et al., 2023). An “old age model” suggests that the initial deposition of the Lulehe Formation occurred in the early Eocene (ca. 43.5–54 Ma; Fang et al., 2007, 2019; Chang et al., 2015; Ji et al., 2017; Xing et al., 2023). In contrast, a “young age model” proposes an Oligocene initial deposition for the Cenozoic strata (ca. 20–25 Ma; Wang et al., 2017, 2022a; Nie et al., 2019; Duan et al., 2022; Lu et al., 2022a, 2022b). The “old age model” is supported by vertebrate fossils, ostracods, spore, and pollen assemblages, (detrital) thermochronological data, and regional lithostratigraphic correlations (Cheng et al., 2021 and references therein). Additionally, biostratigraphy based on Charophyte assemblages (Xing et al., 2023) correlates with the high-resolution magnetostratigraphy of the Paleogene–Neogene sequence (ca. 52–7 Ma; Ji et al., 2017) at the Dahonggou (DHG) Section (Fig. 1C). Recently, carbonate U–Pb dating of syntectonic deposits in the pull-apart East Xorkol basin (Fig. 1C, western Qaidam basin) yielded an age of 58.9 ± 1.29 Ma, providing compelling evidence that the Altyn-Tagh fault initiated its strike-slip motion during the Paleocene–early Eocene (Yi et al., 2024). Additional support for the Eocene initiation viewpoint comes from stable isotope records and long-chain n-alkanes from the DHG section, the ages of interbedded volcanic and tuff rocks from several Eocene sedimentary basins in the northern and eastern Tibetan Plateau, and low-temperature thermochronology results of the Qilian, Altun, and Eastern Kunlun Mountains (Jian et al., 2023, and references therein). The “young age model” is supported by vertebrate fossils, magnetostratigraphy control by mammal fossil assemblages, detrital

zircon geochronologic and detrital apatite thermochronological data (Wang et al., 2017, 2022a; Nie et al., 2019; Duan et al., 2022; Lu et al., 2022a, 2022b). Detailed reviews and comparison analyses of these two age models have been provided by Cheng et al. (2018, 2021, 2023) and Wang et al. (2022b). Although the depositional age of the Cenozoic strata in the Qaidam basin requires further detailed study, this study applies the “old age model” where needed.

The Cenozoic strata in the Qaidam basin consist of evaporite, carbonate, and siliciclastic deposits, predominantly deposited in fluvial-lacustrine sedimentary environments (Jian et al., 2013a, 2013b). Previous studies demonstrate that the Qaidam sedimentary depocenters shifted eastward during the Cenozoic (Bao et al., 2017; Yin et al., 2008), likely due to the uplift of the Eastern Kunlun Mountains (Bao et al., 2017). This results in significant spatial and stratigraphic variations in the Cenozoic lithology (Fig. 3; Jian et al., 2024). The northern and eastern regions of the Qaidam basin are dominated by siliciclastic sedimentary rocks (Fu et al., 2022; Jian et al., 2023; Zhuang et al., 2011), whereas carbonate rocks, evaporite rocks, and mixed carbonate-siliciclastic deposits are common in the western Qaidam basin (Guo et al., 2017; Jian et al., 2014; Zhang et al., 2018). Stratigraphically, the Cenozoic sedimentary succession generally transitions from coarse-grained deposits at the base (E₁₊₂) to relatively fine-grained deposits (E₃, N₁, N₂¹, and N₂²), and then back to coarse-grained deposits (N₂³ and Q₁₊₂) in most areas of the basin (Fig. 3). The coarse-grained strata (E₁₊₂, N₂³, and Q₁₊₂) are interpreted as being dominated by alluvial fan, plain, and marginal lacustrine facies, while the fine-grained strata (E₃, N₁, N₂¹, and N₂²) are associated with fluvial, deltaic, and

lacustrine environments (Fig. 3).

3. Samples and methods

Four sandstone samples (Figs. 1B and 5) were selected for detrital muscovite $^{40}\text{Ar}/^{39}\text{Ar}$ geochronological analysis. Borehole samples L87-02 and L87-09 (Fig. 4) are classified as medium-fine-grained lithic sandstone, whereas borehole sample B1-05 and outcrop sample YCG-20 (Fig. 4) are fine-grained lithic sandstone. These samples had previously been analyzed for petrographic and heavy mineral compositions as well as detrital zircon U-Pb analyses (Jian et al., 2013a, 2023, 2024, Fig. 5). Additionally, samples B1-05 and L87-09 were analyzed for detrital garnet geochemistry (Hong et al., 2020; Jian et al., 2013a), while samples B1-05 and YCG-20 were employed in detrital AFT analyses (Jian et al., 2018, Fig. 5). The detrital framework grains in these samples are angular to subangular and are poorly to moderately sorted (Fig. 2). Quartz and lithic fragments dominate the detrital framework grains, with the lithic fragments primarily consisting of metasedimentary lithic fragments (Jian et al., 2013a). The heavy mineral assemblage includes garnet, epidote, zircon, tourmaline, and apatite, indicating a significant derivation from metamorphic rocks (Jian et al., 2013a).

In preparation for $^{40}\text{Ar}/^{39}\text{Ar}$ isotopic analysis, detrital muscovite grains of 180–280 μm were separated from sandstone samples, cleaned with deionized water, and dried. About 50–60 grains of muscovite were separated from each sample. The muscovite samples, along with standard ZBH-25 biotite (132.9 ± 1.3 Ma; Sang et al., 2006) used for neutron monitoring, and K_2SO_4 and CaF_2 used for K and Ca isotopic revising were packaged together by aluminum foil, sealed in a vacuum quartz bottle and then irradiated in the B4 canal of the 49-2 nuclear reactor at Chinese Institute of Atomic Energy (CIAE), Beijing. Muscovite laser

$^{40}\text{Ar}/^{39}\text{Ar}$ analyses were conducted at the Key Laboratory of Orogenic Belts and Crustal Evolution, Peking University. After irradiation, the samples were analyzed by using the automatic high-precision and high-resolution laser microprobe $^{40}\text{Ar}/^{39}\text{Ar}$ dating system (Zhou et al., 2008; Xu et al., 2013). The muscovite samples and monitors were degassed and fused by a New Wave CO_2 laser. The argon isotopes were measured by using a VG5400 mass spectrometer. About 50 unknown grains were analyzed per sample. The $^{40}\text{Ar}/^{39}\text{Ar}$ ages were calculated based on the argon isotopic ratios measured after corrections for mass discrimination, interfering nuclear reactions, procedural blanks, and atmospheric Ar contamination. The procedures for isotopic analyses and age calculations were controlled by MassSpec software (Deino, 2010).

4. Results

In total, we report 194 new detrital single-grain muscovite $^{40}\text{Ar}/^{39}\text{Ar}$ ages from the four samples. The ages range from 210 Ma to 490 Ma and have a major age group of 300–400 Ma and minor groups of 250–270 Ma and ca. 500 Ma (Fig. 6). Specifically, sample L87-02 from the E_3 strata yields detrital muscovite ages range from 210 Ma to 430 Ma, with a major age group of 280–410 Ma (Fig. 6E). Ages of the N_1 sample YCG-20 are distributed between 250 Ma and 460 Ma with a major age group of 280–430 Ma (Fig. 6D). The N_1 sample L87-09 yields an age distribution from 290 Ma to 390 Ma, with a major age group of 320–390 Ma (Fig. 6C). Ages of sample B1-05 from the N_2^2 strata covers a range from 250 Ma to 490 Ma, with a major age group of 380–410 Ma (Fig. 6B).

The compilation indicates that detrital muscovite grains from the Lulehe (LLH) Section (Fig. 1C) in the northern Qaidam basin yield a uniform Permian $^{40}\text{Ar}/^{39}\text{Ar}$ age group of 250–279 Ma (Fig. 7; Rieser et al., 2006a). In the western Qaidam basin, detrital muscovite $^{40}\text{Ar}/^{39}\text{Ar}$ dating reveals several age groups, including ca. 350–450 Ma and ca.

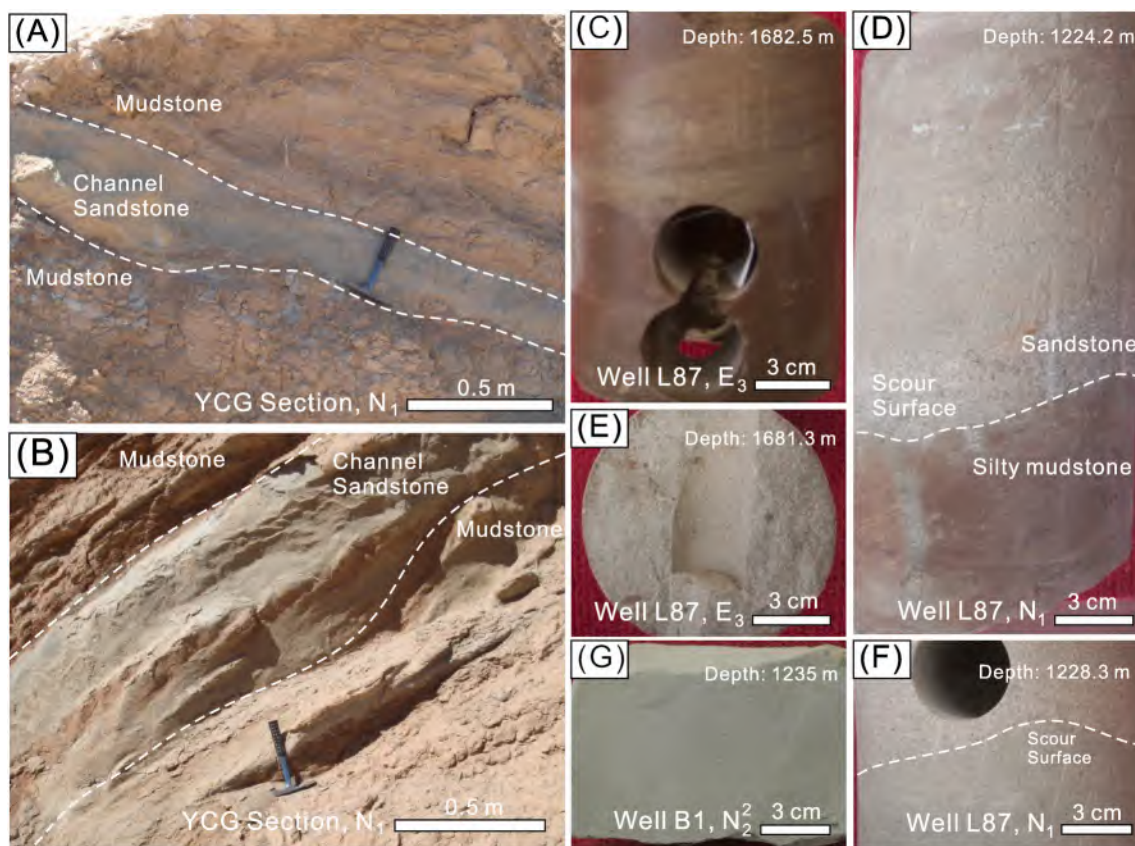


Fig. 4. Representative photographs of sedimentary rocks of the Xiaganchaigou Fm. (E_3), Shangganachaigou Fm. (N_1), and Shangyoushashan Fm. at the YCG Section and wells L87 and B1 in the northern Qaidam basin (locations see Fig. 1C). (A–B) YCG Section; (C–F) well L87; (G) well B1.

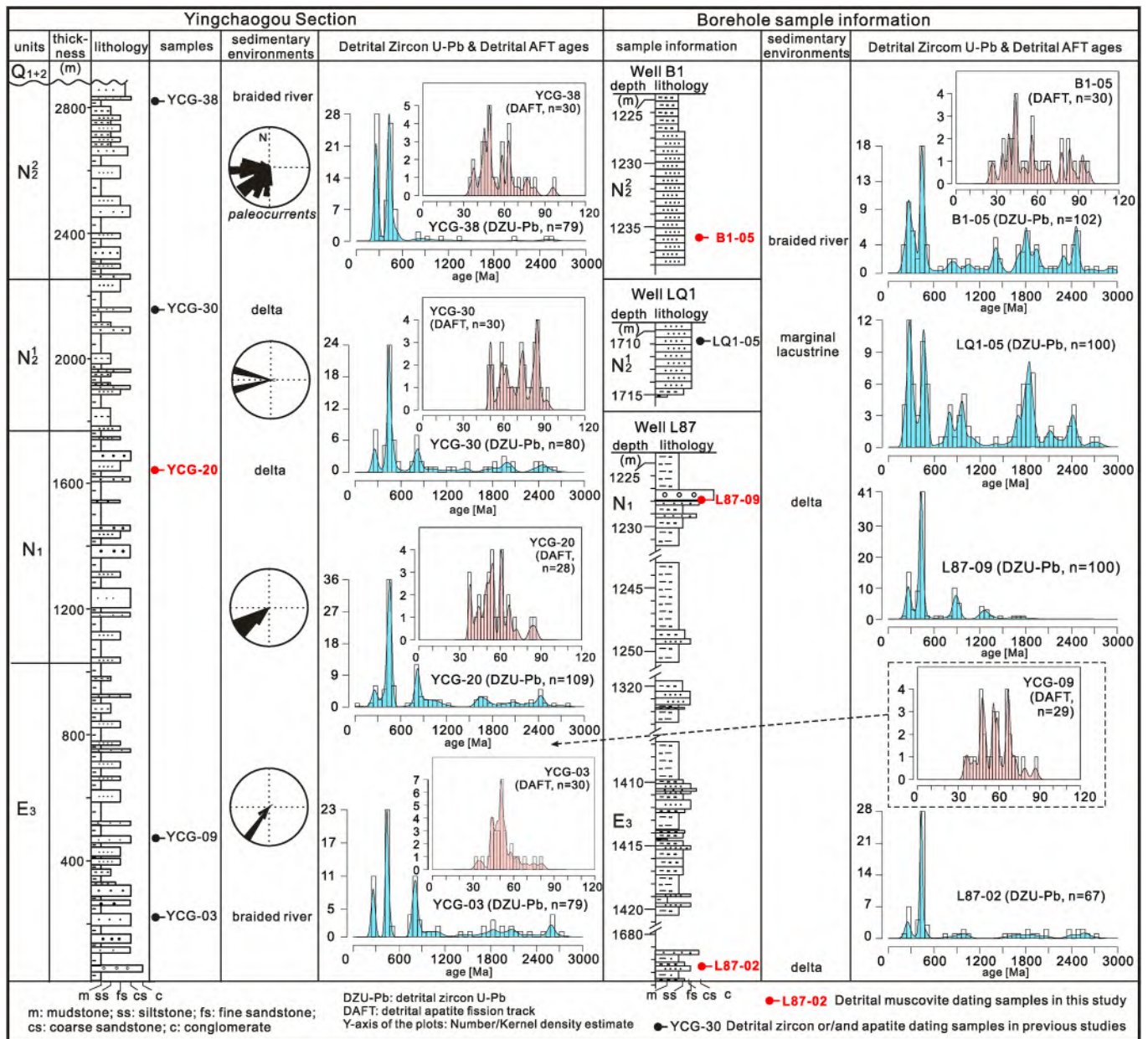


Fig. 5. Stratigraphic columns of the analyzed outcrop section and drilling cores and previously published data, modified from Jian et al. (2024). The samples marked as red names were selected for detrital muscovite $^{40}\text{Ar}/^{39}\text{Ar}$ geochronology in this study. Detrital zircon U-Pb results are from Jian et al. (2024). Paleocurrent data and detrital apatite fission track results are from Jian et al. (2018).

220–280 Ma, with subordinate clusters of ca. 122–140 Ma and a minor group ca. 500 Ma. The age range between 350 and 450 Ma is the most common and dominant (Fig. 8; Rieser et al., 2006b, 2007). Another study on detrital muscovite $^{40}\text{Ar}/^{39}\text{Ar}$ dating for the E₃ and N₁ stata of the Hongsanhan (HSH) Section (Fig. 1C) in the western Qaidam presents a major age group of ca. 30–340 Ma (Wang, 2023).

5. Discussion

5.1. Provenance of the Cenozoic deposits in the Qaidam basin: A review

Studies from distinct target perspectives, such as bed load, suspended load, and dissolved load, focus on different mediums and may draw diverse conclusions on the provenance of the Cenozoic Qaidam basin. From the perspective of relatively coarse grains which are commonly transported by bed loads, petrographic analyses show that most of the

Cenozoic sandstones are relatively immature in both texture and composition. Specifically, detrital grains in most sandstones are mainly angular to subangular, poorly to moderately sorted, and contain abundant lithic fragments (Fig. 2; Rieser et al., 2005; Jian et al., 2013a; Bush et al., 2016; McRivette et al., 2019; Sun et al., 2020a). This indicates that the sandstones were mainly derived from nearby source terranes (Jian et al., 2013a; Rieser et al., 2005). The sandstone point-count modal data suggest predominant recycled-orogeny and collisional sutures & fold-thrust belt sources (Rieser et al., 2005; Jian et al., 2013a; Bush et al., 2016; McRivette et al., 2019; Lu et al., 2018; Fu et al., 2022). The framework grain compositions exhibit slight spatial variation in the northern Qaidam basin (Jian et al., 2013a) and minor changes over time in the western Qaidam basin (Rieser et al., 2005). Heavy minerals are dominated by zircon, tourmaline, rutile, apatite, epidote, garnet, hornblende, hematite, and magnetite, indicating that the source terranes comprise intermediate-acidic igneous rocks and medium-to low-grade

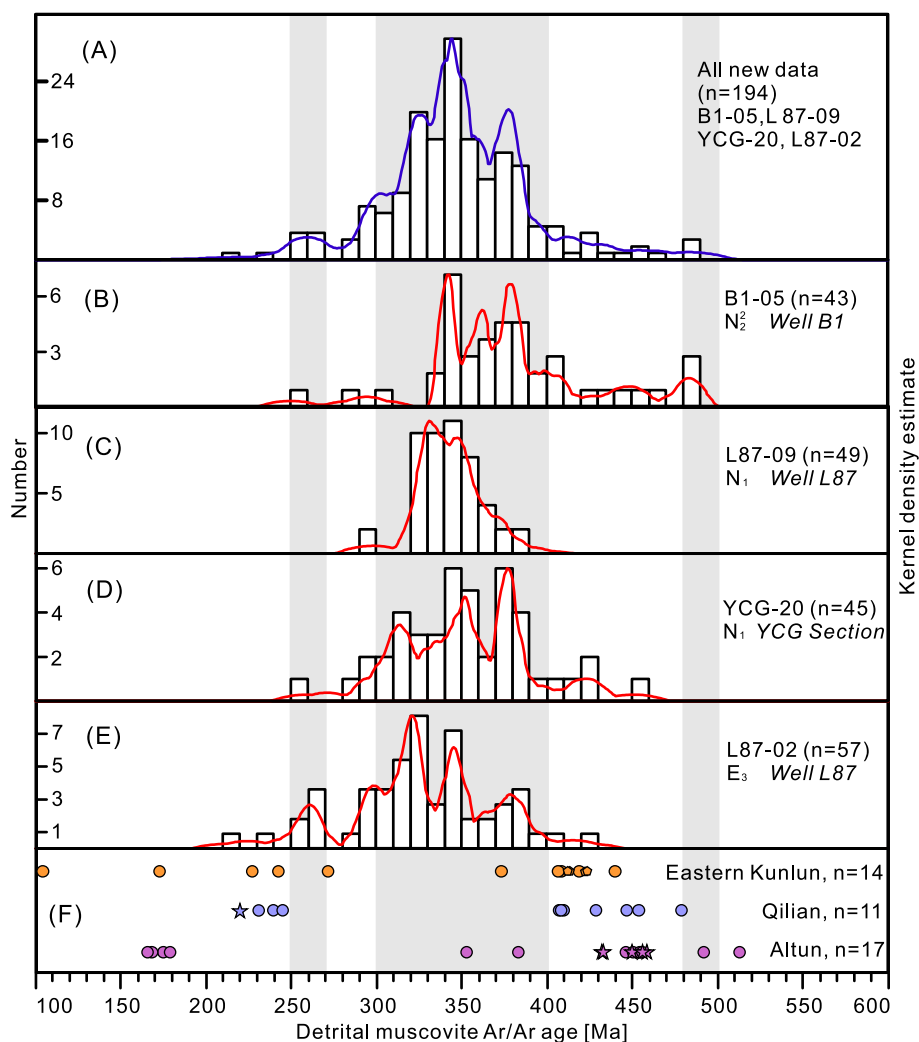


Fig. 6. Kernel density estimate (KDE) curves and histograms for detrital muscovite $^{40}\text{Ar}/^{39}\text{Ar}$ geochronologic results of the Cenozoic sandstone samples from the northern Qaidam basin. (A) KDE curves and histograms for all our new data. (B) KDE curves and histograms for sample B1-05. (C) KDE curves and histograms for sample L87-09. (D) KDE curves and histograms for sample YCG-20. (E) KDE curves and histograms for sample L87-02. (F) Muscovite $^{40}\text{Ar}/^{39}\text{Ar}$ ages of potential source terranes. The circle represents metamorphic rocks, the pentagon represents dike rocks, and the pentagram represents magmatic rocks. Shaded bars point out the 250–270 Ma, the 300–400 Ma, and the ca. 500 Ma intervals. References and locations of ages in three mountain ranges see Fig. 1B.

metamorphic rocks or slightly metamorphic clastic rocks (Jian et al., 2013a; Zhu et al., 2017; Zhou et al., 2018; Nie et al., 2019; Ding et al., 2022). Detrital zircon U-Pb age signatures of the western basin are characterized by 400–480 Ma and 220–280 Ma with minor Precambrian signals, indicating major contributions from the neighboring Altun and Eastern Kunlun ranges (Fig. 10; e.g., Bush et al., 2016; Cheng et al., 2016; Wang et al., 2017, 2022a; Jian et al., 2024 and references therein). However, detrital zircon records in the northern and eastern basin display prominent early Paleozoic U-Pb ages with relatively significant Paleoproterozoic, Neoproterozoic, and Permian–Triassic signals in some samples (Fig. 10; e.g., Bush et al., 2016; Cheng et al., 2016; Wang et al., 2017, 2022a; Jian et al., 2024 and references therein). The observed different temporal variation trends in detrital zircon records from the northern basin are thought to be due to variable zircon supply from different micro-terranes in the Qilian Mountains (Fig. 10; e.g., Bush et al., 2016; Cheng et al., 2016; Wang et al., 2017, 2022a; Jian et al., 2024 and references therein). Detrital AFT ages of previously analyzed sandstones also display high spatial variations (Fig. 11; e.g., Wang et al., 2017, 2022a; Jian et al., 2018; He et al., 2021a, 2021b). The northern Qaidam basin indicates two kinds of detrital AFT age distributions: ca. 20 Ma to ca. 100 Ma in the western region and ca. 5 Ma to ca. 200 Ma in the eastern region and the ages of the western Qaidam basin range from

ca. 20 Ma to ca. 160 Ma (Wang, 2023).

Mudstone and siltstone analyses may provide valuable insights into the provenance of fine grains that are commonly transported by suspended loads. Geochemical studies on mudstone indicate that sediments were primarily derived from a source area dominated by acidic-intermediate rocks (Jian et al., 2013b; Bao et al., 2019; Sun et al., 2020b; Li et al., 2021). The $^{87}\text{Sr}/^{86}\text{Sr}$ ratios and $^{143}\text{Nd}/^{144}\text{Nd}$ ratios of mudstone silicate fractions from the Cenozoic strata in the northern Qaidam basin indicate that the fine-grained sediments were primarily derived from the Qilian Mountains (Yan et al., 2024). Furthermore, fine-grained sediments may be affected by sediment transport pathways and water dynamics, such as lake currents, especially in paleo-megalakes. This results in well-mixed composition of sediments from various source terranes (Ren et al., 2019; Wang et al., 2023). Paleowater solute Sr isotope studies, based on authigenic carbonate fractions, provide insights into dissolved load (Yang et al., 2016, 2022; Liu et al., 2022, 2023; Yan et al., 2024). The $^{87}\text{Sr}/^{86}\text{Sr}$ ratios in paleowater solutes from the northern Qaidam basin have been remarkably high since ca. 54 Ma, suggesting a Qilian-dominated source (Liu et al., 2023; Yan et al., 2024). Given that the $^{87}\text{Sr}/^{86}\text{Sr}$ ratios in Eastern Kunlun Mountains are significantly lower (Yang et al., 2022; Liu et al., 2023; Yan et al., 2024), the relatively low paleowater solute $^{87}\text{Sr}/^{86}\text{Sr}$ ratios

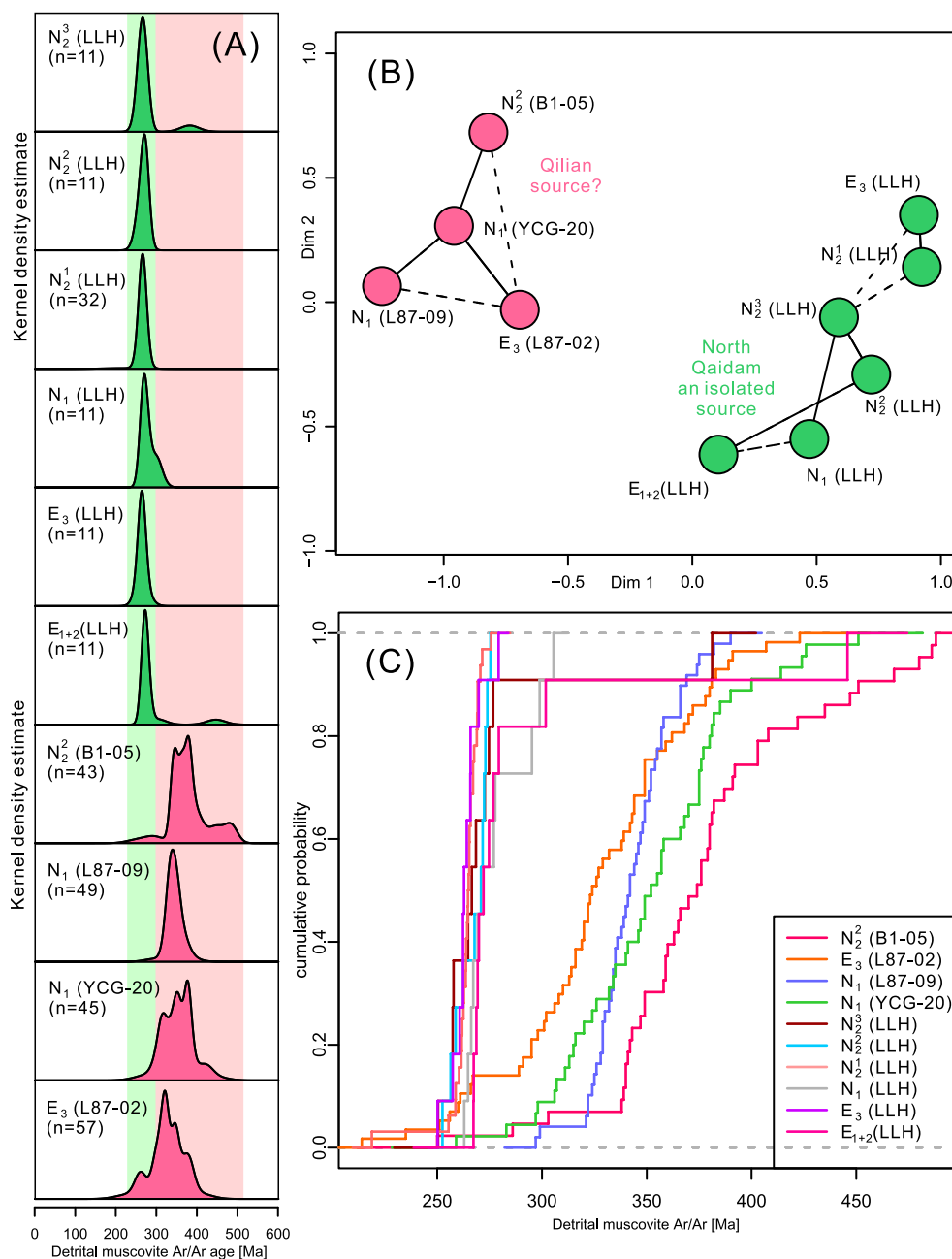


Fig. 7. KDE curves (A), non-metric multidimensional scaling (MDS) plots (B), and Cumulative probability plots (C) for detrital muscovite $^{40}\text{Ar}/^{39}\text{Ar}$ ages from the northern Qaidam basin. LLH, Lulehe Section. Data of the LLH Section are from Rieser et al. (2006a). The R programming language-based Provenance software (Vermeesch et al., 2016) was employed for the illustrations.

during the paleo-megalake periods (ca. 44.5 to ca. 32 Ma and after ca. 16 Ma; Liu et al., 2023) likely indicate the well-mixing of materials derived from both the Qilian and Eastern Kunlun Mountains (Liu et al., 2023).

In summary, the above-mentioned analysis of sedimentary samples combined with paleo-flow direction measurement results (Zhuang et al., 2011; Wu et al., 2012b; Bush et al., 2016; Xia et al., 2020; Lu et al., 2022b) suggests that the expansive northern and eastern regions of the Qaidam basin were primarily fed by the Qilian Mountains. In contrast, the Altun and Eastern Mountains were the major sources of the Cenozoic sedimentary rocks in relatively limited western Qaidam regions (Rieser et al., 2005, 2006a, 2006b; Zhuang et al., 2011; Jian et al., 2013a, 2024; Liu et al., 2022, 2023). During the paleo-megalake periods, fine-grained sediments and solute materials from these different source terranes may have mixed through lake currents or other water dynamics (Liu et al.,

2022, 2023; Wang et al., 2023). Additionally, tectonic evolutions of the surrounding mountains, climate change, and variations in the sediment source-to-sink system contributed to the high spatiotemporal variability in detrital compositions within the Cenozoic Qaidam basin (Cheng et al., 2021; Jian et al., 2024). This variability indicates that the Cenozoic provenance of the Qaidam basin still needs to be rigorously inspected.

5.2. Cenozoic Qaidam basin detrital muscovite $^{40}\text{Ar}/^{39}\text{Ar}$ age distributions, controls, and muscovite provenance interpretations

The compilation results of detrital muscovite $^{40}\text{Ar}/^{39}\text{Ar}$ ages, including our new data, reveal that the Cenozoic deposits from the Qaidam basin (excluding the LLH section) are predominantly characterized by ages of 300–400 Ma, with minor groups of 200–300 Ma and sparse occurrences of 400–500 Ma (Figs. 7 and 8).

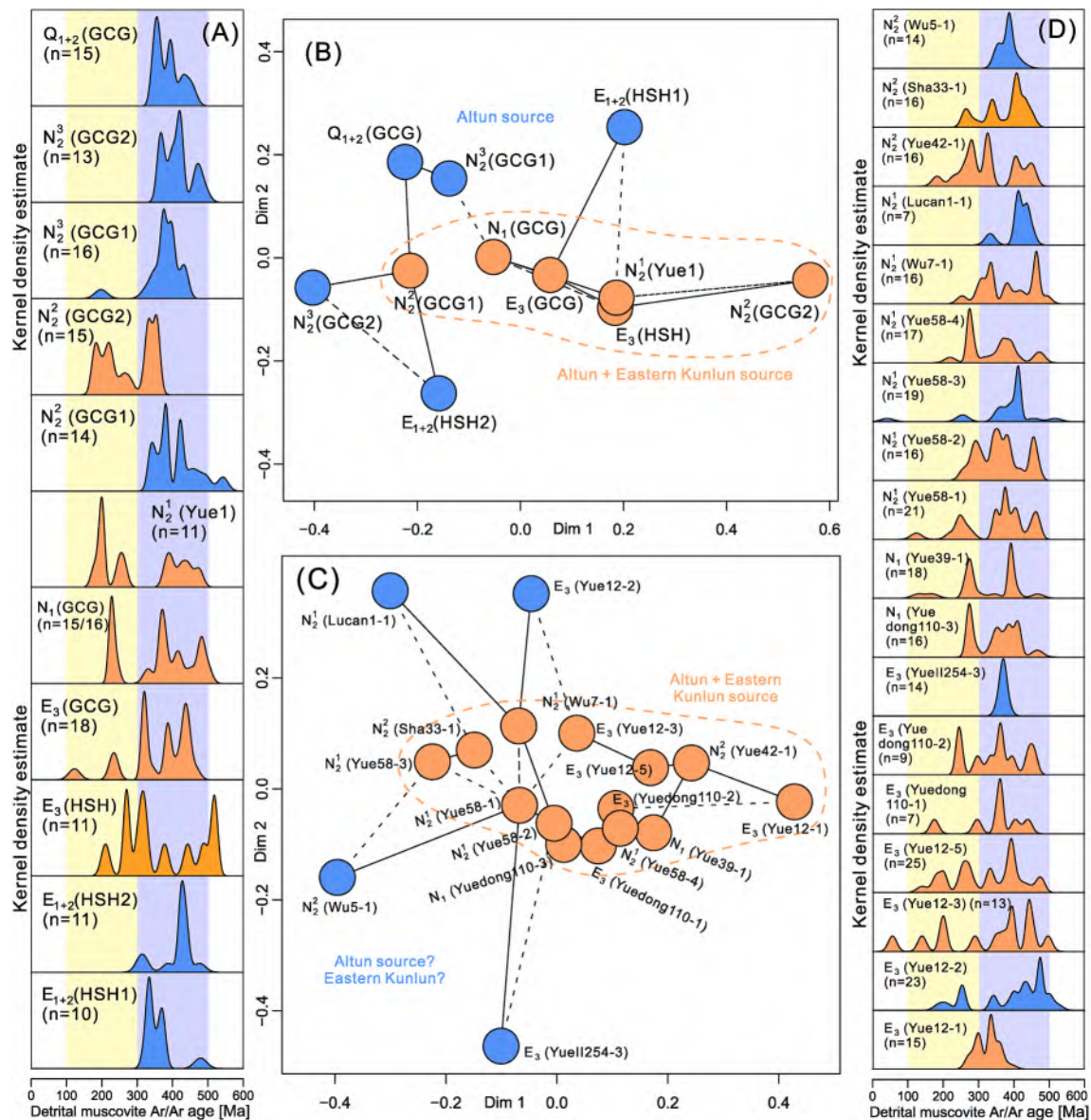


Fig. 8. KDE curves (A) and MDS plots (B) for detrital muscovite $^{40}\text{Ar}/^{39}\text{Ar}$ ages from GCG and HSH Sections and drilling well Yue1. MDS plots (C) and KDE curves (D) for detrital muscovite $^{40}\text{Ar}/^{39}\text{Ar}$ ages from drilling wells located in the western Qaidam basin. Data are from Rieser et al. (2006b, 2007, 2010). The R programming language-based Provenance software (Vermeesch et al., 2016) was employed for the illustrations.

Our new samples from the northern Qaidam basin show a dominant detrital muscovite age group of 300–400 Ma (Figs. 6 and 7). As mentioned above, the Qilian Orogen has been thought to be the main source of the northern Qaidam basin deposits (Rieser et al., 2005, 2006a; Zhuang et al., 2011; Jian et al., 2013a, 2024; Liu et al., 2022, 2023). It contains abundant metamorphic sedimentary rocks (Fu et al., 2022; Gehrels et al., 2003a, 2003b; Jian et al., 2013a, 2018, 2024; Rieser et al., 2005; Wang et al., 2023) and may have high muscovite fertility. Consequently, the detrital muscovite grains of our samples in the northern basin were likely derived from the Qilian Orogen and may be related to the Devonian–Carboniferous cooling history of the North Qaidam orogenic belt (Song et al., 2005). However, there is a lack of muscovite $^{40}\text{Ar}/^{39}\text{Ar}$ records with 300–400 Ma from the potential source areas (Figs. 1A and 6F), and modern river sediments in the north margin of the Qaidam basin show only a few grains with these ages (Genser et al., 2010). This discrepancy may be due to the limited application of muscovite $^{40}\text{Ar}/^{39}\text{Ar}$ dating in the North Qaidam region, hindering a direct comparison between source (Qilian Orogen) and sink (Cenozoic Qaidam basin). Samples from the LLH Section, in the northern Qaidam

basin, display a unique detrital muscovite age range of 250–279 Ma (Fig. 7; Rieser et al., 2006a), which is dramatically different from the others. The Cenozoic lithology of the LLH section (Jian et al., 2013a), isopach maps of the Cenozoic strata (Bao et al., 2017; Cheng et al., 2021), and the paleogeography of the LLH area (Li, 2022) suggest that the LLH area was located far away from the depocenter and was dominated by the alluvial fan, fluvial, and delta sedimentary environments during the Cenozoic. This means that detrital muscovite grains in the LLH area may be derived from a solitary proximal source terrane with Permian–Triassic muscovite $^{40}\text{Ar}/^{39}\text{Ar}$ ages in the Qilian Orogen.

Two major detrital muscovite age groups have been identified in the western Qaidam basin, namely, 200–300 Ma and 300–500 Ma (Fig. 8). The Altun and Qimantagh Orogens are considered the primary Cenozoic sources for this region (Rieser et al., 2006b; Zhu et al., 2017, 2019; Cheng et al., 2015, 2016, 2021). Muscovites with ages of ca. 270 and 400 Ma have been reported in the Qimantagh Orogens (Fig. 1B; Feng et al., 2013; Bontje, 2015; Guo et al., 2012; Zheng et al., 2016), and ages between 350 and 500 Ma and ca. 170 Ma have been found in the Altun Orogens (Figs. 1B and 6F; Sobel and Arnaud, 1999; Liu et al., 2003,

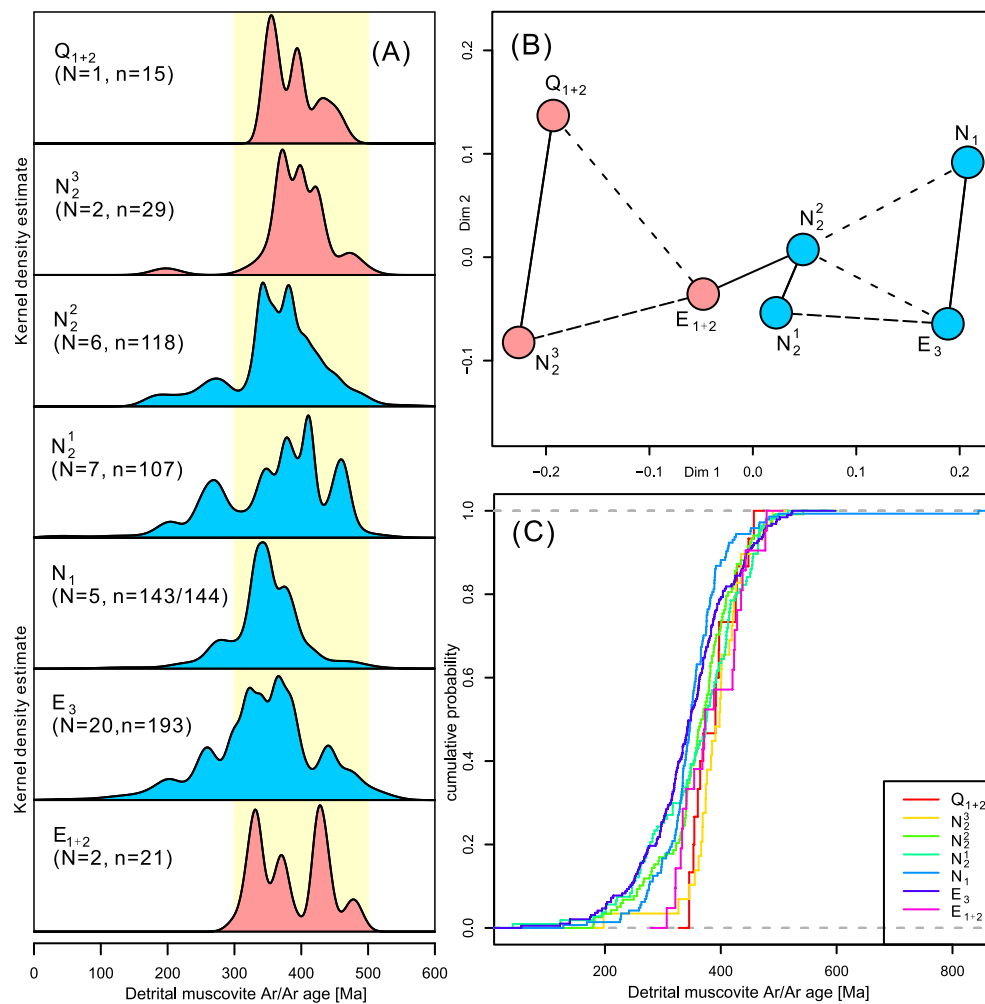


Fig. 9. KDE curves (A), MDS plots (B), and cumulative probability plots (C) of detrital muscovite $^{40}\text{Ar}/^{39}\text{Ar}$ age from different Cenozoic strata of the Cenozoic Qaidam basin. N, number of samples; n, number of dated detrital muscovite grains. Data are from Rieser et al. (2006b, 2007, 2010) and this study. The R programming language-based Provenance software (Vermeesch et al., 2016) was employed for the illustrations. We realize that the numbers of the combined ages of the E_3 , N_1 , N_2^1 , and N_2^2 strata are much more than those of the E_{1+2} , N_2^3 , and Q_{1+2} strata. Here, we employed sensitivity analyses to test the geological meaning of these relatively wide age ranges (see Appendix B for details). The results show that for each formation, almost all the samples have similar sensitivity to the age ranges of combined data (Figs. S4–S7). The combined data exhibits a wider age range because most of the samples have wide age ranges, rather than large sample sizes.

2007; Zhang et al., 2007). The locations of the HSH and the GCG Sections and the drilling well Yue1 are close to the Altun Orogen (Fig. 1B and C). Therefore, the detrital muscovite grains with ages of 300–500 Ma in these areas may be derived from the Altun Orogen (Fig. 8A and B). These ages may be related to the Paleozoic subduction-collisional and subsequent cooling process of this orogen. The detrital muscovite grains with 200–300 Ma ages in these areas may be provided by the Qimantagh Orogen and documented late Paleozoic to early Mesozoic subduction-collisional and subsequent cooling processes. Samples with age groups of 200–340 Ma from the HSH Section (the E_3 and N_1 strata; Wang, 2023) may be also associated with these tectonic events. Samples from drilling wells located in the Qimantagh foreland, the western Qaidam basin (Fig. 1C) show a wider age range (Fig. 8C and D), indicating a broader mixing of detrital muscovite grains from both the Altun and Qimantagh Orogens.

The available data demonstrate that the Cenozoic deposits exhibit stratigraphically various detrital muscovite age ranges (Fig. 9). Most samples from the E_3 , N_1 , N_2^1 , and N_2^2 strata have relatively wider age ranges compared to those from the E_{1+2} , N_2^3 , and Q_{1+2} strata (Fig. 8; Rieser et al., 2006b). Although the number of the available detrital muscovite $^{40}\text{Ar}/^{39}\text{Ar}$ dating grains varies significantly among these stratigraphic units, sensitivity analysis results (Figs. S4–S7 in Appendix

B) indicate that these differences in detrital muscovite records are not due to sample sizes and the number of analyzed grains. We recognize that the E_{1+2} , N_2^3 , and Q_{1+2} strata in the Qaidam basin are mainly composed of relatively coarse-grained deposits, while the E_3 – N_2^2 strata are dominated by fine-grained deposits, indicative of alluvial-fluvial and deltaic-lacustrine sedimentary environments, respectively (Fig. 3). It is also observed that detrital muscovite grains are likely to transport with silt and mud by suspended loads (Jirí, 2009; Stuart, 2002; Malusà and Garzanti, 2019), suggesting that their transport pathways may be more complex than those of sandy sediments within the same sedimentary depocenter (Malusà and Garzanti, 2019; Shen et al., 2021; Wang et al., 2023). Consequently, we advocate that various transport processes in distinct sedimentary environments likely control the detrital muscovite age distributions over time. This interpretation is reinforced by the mega-lake proposition (Liu et al., 2022, 2023; Wang et al., 2023), which suggests that fine-grained sediments (transported by suspended loads, such as clay minerals and detrital muscovite grains) from different source terranes may be transported through lake currents and thoroughly mixed (Fig. 13), resulting relatively wide detrital muscovite age ranges in the fine-grained deposits (Figs. 8 and 9). Furthermore, our four samples (Fig. 7) and several previous samples (Fig. 8; Rieser et al., 2006b) from the fine-grained deposits exhibit narrower age ranges than

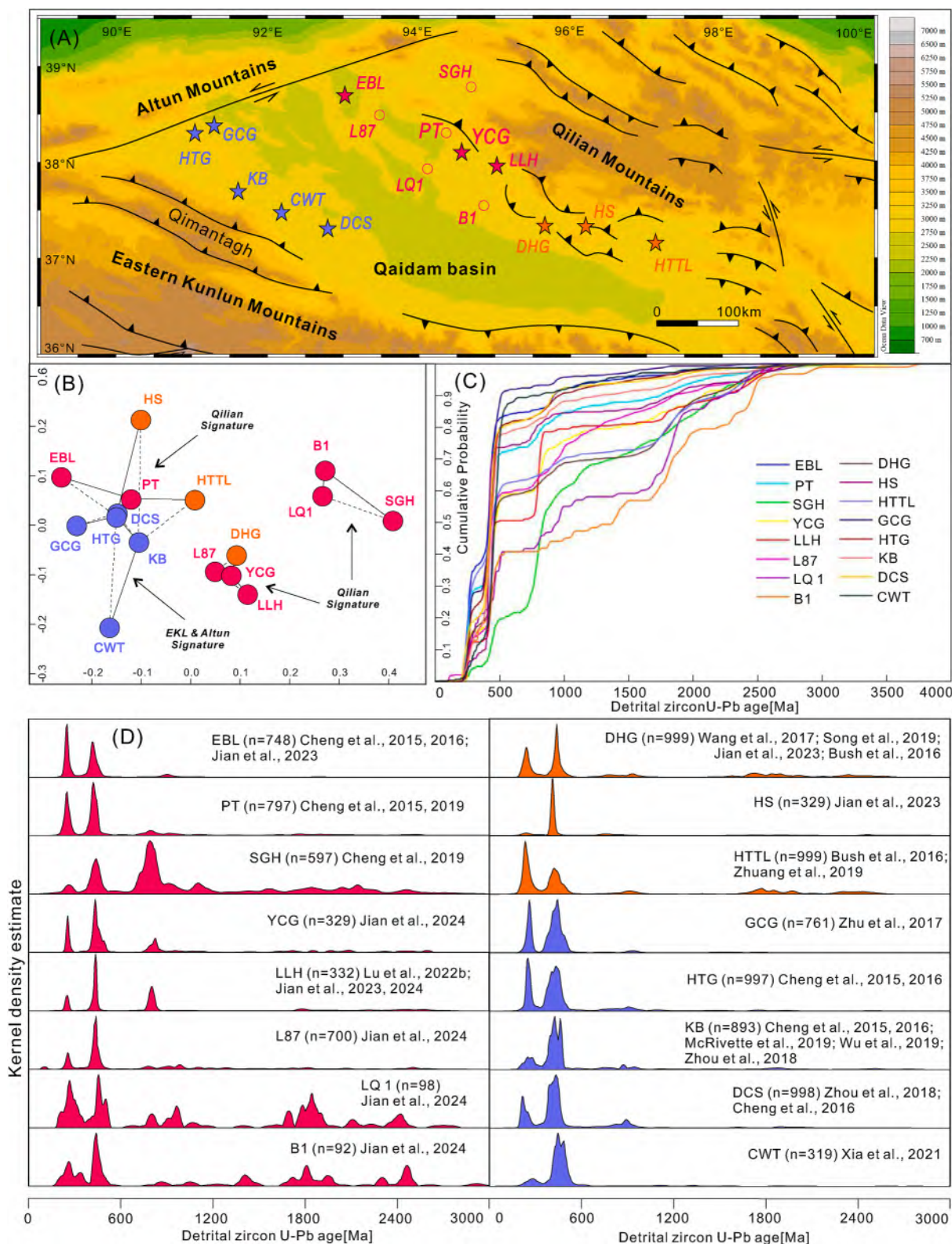


Fig. 10. (A) Topographic map of the Qaidam basin with locations of published detrital zircon studies. (B) MDS plots for published detrital zircon U-Pb age of the Cenozoic Qaidam basin. (C) Published detrital zircon U-Pb age cumulative probability curves of the Cenozoic Qaidam basin. (D) KDE curves for published detrital zircon U-Pb age of the Cenozoic Qaidam basin. Ages <1000 Ma are based on initial-Pb corrected $^{206}\text{Pb}/^{238}\text{U}$ ratios, whereas ages >1000 Ma are based on initial-Pb corrected $^{206}\text{Pb}/^{207}\text{Pb}$ ratios. Data are from Bush et al. (2016); Cheng et al. (2015, 2016, 2019b); Jian et al. (2023, 2024); Li et al. (2021); Lu et al. (2022b); McRivette et al. (2019); Pullen et al. (2011); Sun et al. (2020a); Wang et al. (2017); Wu et al. (2019b); Xia et al. (2020); Yin et al. (2020); Zhou et al. (2018); Zhu et al. (2017, 2019); Zhuang et al. (2019). The R programming language-based Provenance software (Vermeesch et al., 2016) was employed for the illustrations.

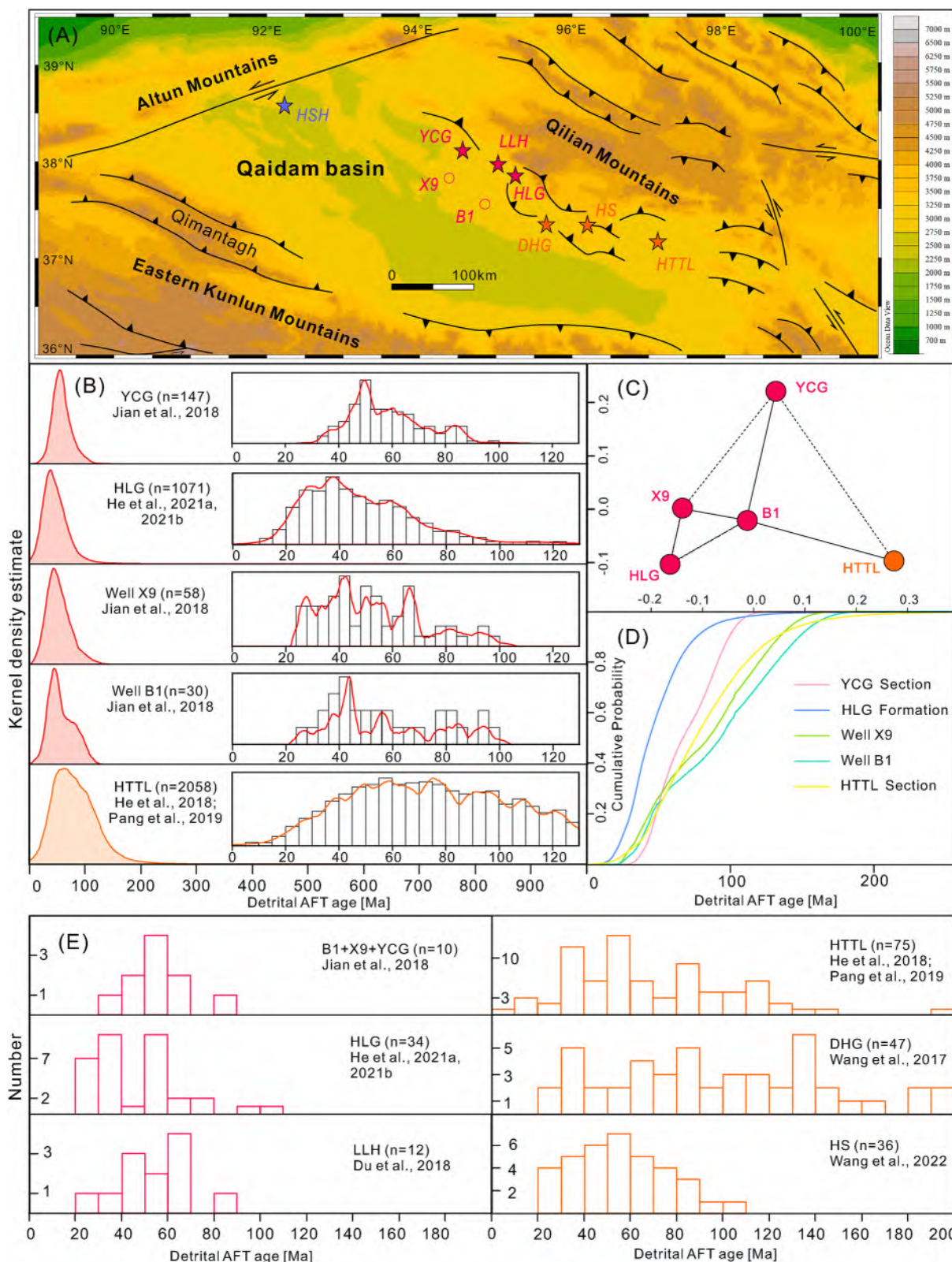


Fig. 11. (A) Topographic map of the Qaidam basin with locations of published detrital apatite studies. (B) KDE curves and histograms for published detrital apatite studies of the Cenozoic Qaidam basin. (C) MDS plot for published detrital apatite fission track (AFT) age of the Cenozoic Qaidam basin. (D) Published detrital AFT age cumulative probability curves of the Cenozoic Qaidam basin. (E) Histograms for published detrital AFT peak ages. Data are from [Du et al. \(2018\)](#); [He et al. \(2018, 2021a, 2021b\)](#); [Jian et al. \(2018\)](#); [Lu et al. \(2022a\)](#); [Pang et al. \(2019\)](#); [Wang et al. \(2017\)](#); [Yin et al. \(2002\)](#). The R programming language-based Provenance software ([Vermeesch et al., 2016](#)) was employed for the illustrations.

others (Figs. 7 and 8; Figs. S1 and S2 in Appendix B). We observed that our samples are fine-to medium-grained sandstones (Fig. 2 and Fig. S2); the samples from the E₃, N₁, N₂¹, and N₂² strata in the GCG section are siltstones (Rieser et al., 2007); and samples from the N₂³, and Q₁₊₂ strata in the HSH and the GCG sections are medium-grained sandstones (Fig. S2; Rieser et al., 2007). This indicates that samples (host clastic rocks) with coarser grain sizes may have narrower detrital muscovite age ranges compared to samples with finer grain sizes.

5.3. Comparison of the Cenozoic Qaidam basin detrital muscovite, apatite, and zircon records and their source-to-sink behaviors

Our data compilation indicates that the detrital zircon U-Pb age spectra have the oldest ages, the widest age ranges, and the largest number of age groups, followed by the detrital muscovite ⁴⁰Ar/³⁹Ar and AFT age spectra (Fig. 12). This can be explained by the tectonic history of source terranes, closure temperature, and mineral weathering resistance (Figs. 12 and 13; Carrapa, 2010; Hodges et al., 2005; Stuart, 2002). The inheritance of detrital zircon is well known and has been broadly involved in detrital zircon provenance interpretations. Due to the high closure temperature of the U-Pb isotopic system and its strong

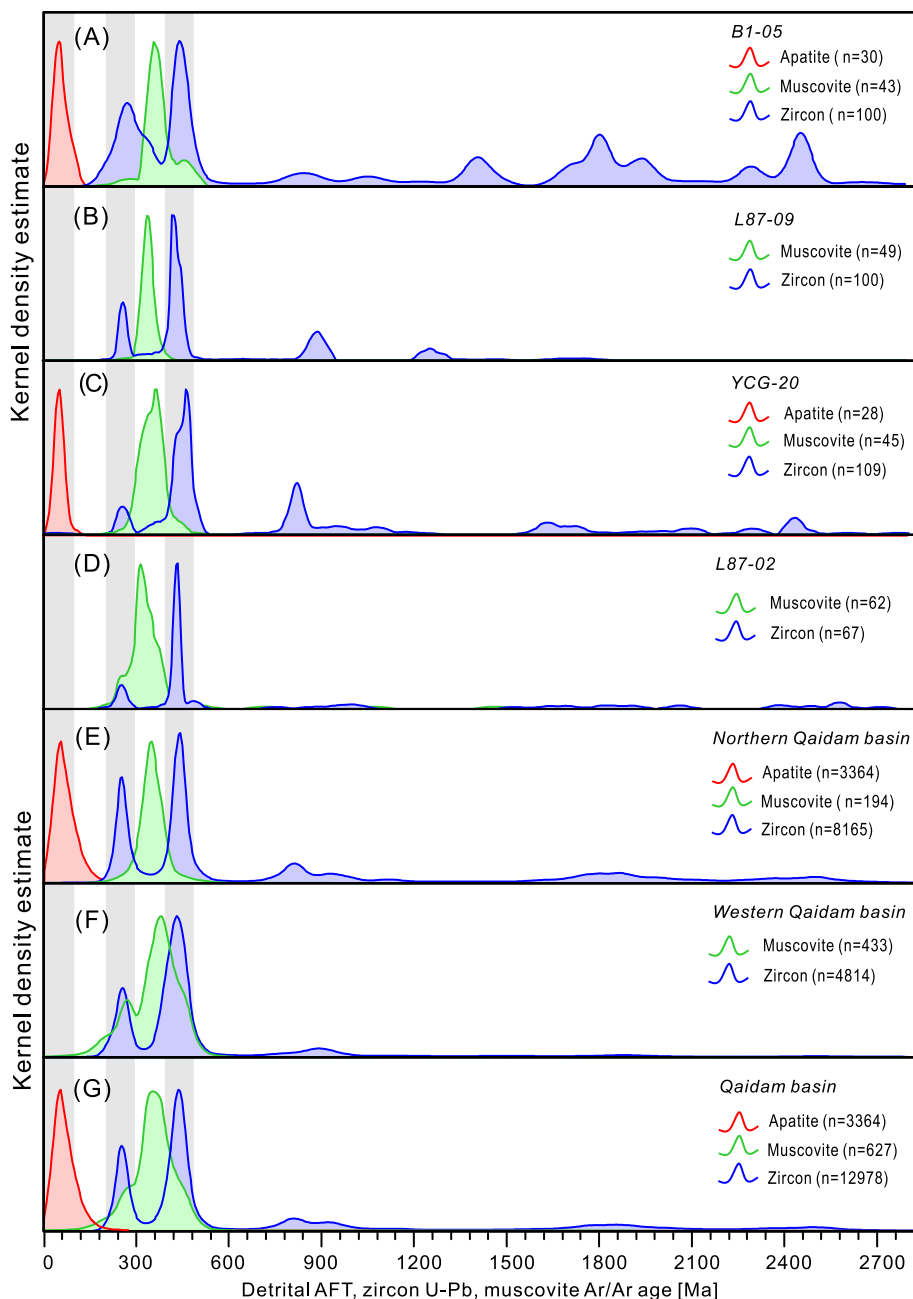


Fig. 12. (A) KDE curves for detrital muscovite ⁴⁰Ar/³⁹Ar, detrital zircon U-Pb, and detrital AFT ages of sample B1-05. (B) KDE curves for detrital muscovite ⁴⁰Ar/³⁹Ar and detrital zircon U-Pb ages of sample L87-09. (C) KDE curves for detrital muscovite ⁴⁰Ar/³⁹Ar, detrital zircon U-Pb, and detrital AFT ages of sample YCG-20. (D) KDE curves for detrital muscovite ⁴⁰Ar/³⁹Ar and detrital zircon U-Pb ages of sample L87-02. (E) KDE curves for detrital muscovite ⁴⁰Ar/³⁹Ar, detrital zircon U-Pb, and detrital AFT ages from the northern Qaidam basin. (F) KDE curves for detrital muscovite ⁴⁰Ar/³⁹Ar, detrital zircon U-Pb, and detrital AFT ages from the western Qaidam basin. (G) KDE curves for all detrital muscovite ⁴⁰Ar/³⁹Ar, detrital zircon U-Pb, and detrital AFT ages from the Qaidam basin. The R programming language-based Provenance software (Vermeesch et al., 2016) was employed for the illustrations.

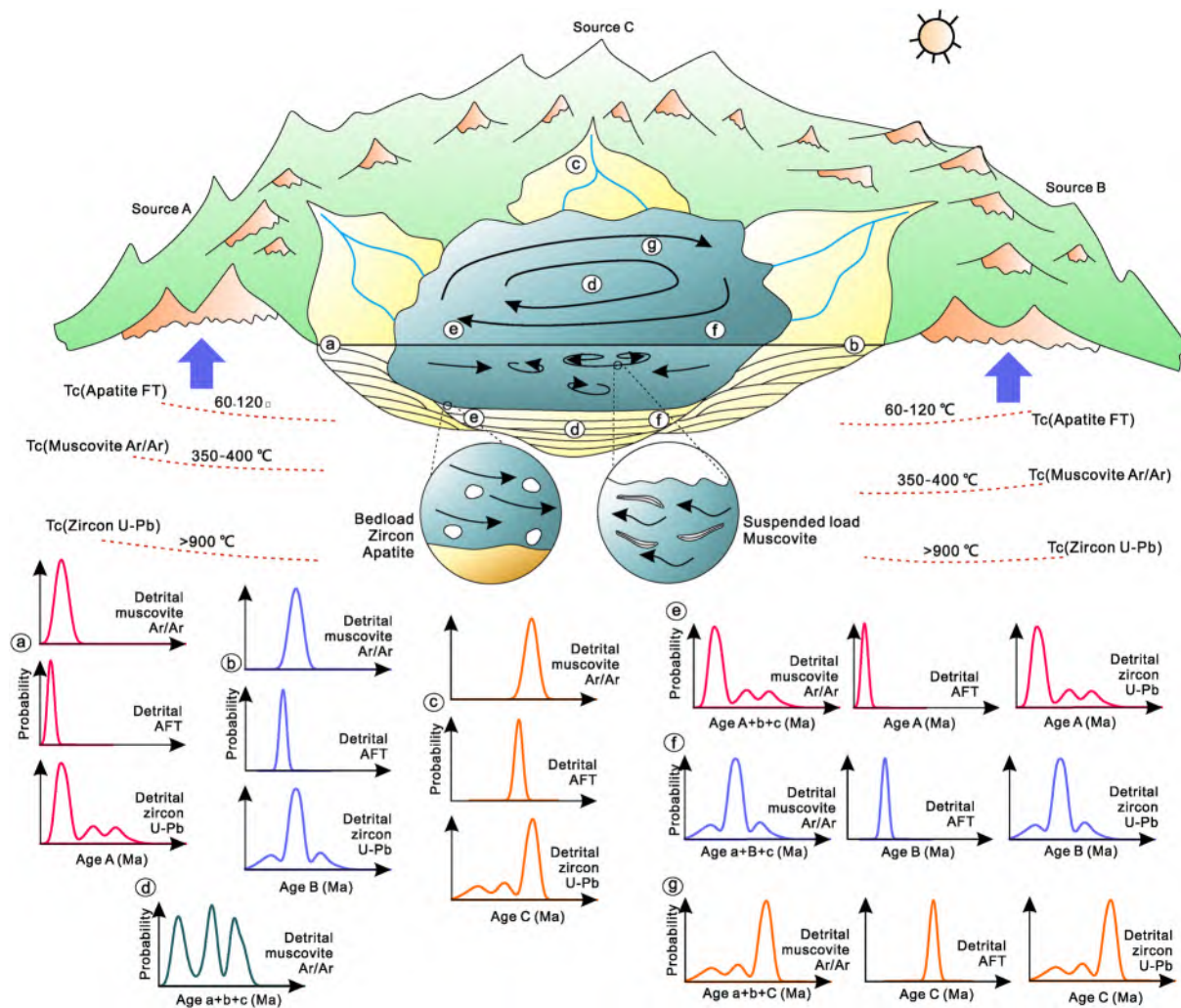


Fig. 13. Schematic model showing the different source-to-sink behaviors of detrital muscovite, zircon, and apatite. Spectra a, b, & c show the age distributions of proximal and relatively coarse-grained sedimentary environments. Spectrum d shows the remote fine-grained sedimentary environments that accelerate the mixing of detrital muscovites and result in a wide age range with symmetry age groups. The granular-shape detrital zircon and apatite might be absent from the spectra like spectrum d because they would be commonly transported by bed load and likely to deposit proximally. Spectra e, f, & g of detrital muscovite records show the part mixing of detrital muscovite grains and ages. The muscovites are dominated by the grains that came from nearby source terrane with a few grains from another source terranes. The spectra e, f, & g of detrital zircon and apatite might be similar to the spectra a, b, & c for the same reason as the absence of the spectra like spectrum d.

resistance to weathering (Hodges et al., 2005; von Eynatten and Dunkl, 2012), detrital zircon records would not be lost during multiple sedimentary cycles (Dickinson et al., 2009). This means that detrital zircons with distinct age groups associated with different tectonic-magmatic histories may be transported to the same deposition area, producing a wide age range and numerous age groups in detrital zircon records. In contrast, due to their low weathering resistance (relative to zircon) and low closure temperature, the records involving muscovite and apatite can only survive from the first or relatively few sedimentary cycles (Stuart, 2002; von Eynatten and Dunkl, 2012).

The 360–540 Ma group of detrital zircons from the Cenozoic Qaidam basin may be associated with the Proto-Tethys Ocean subduction-collision events, which are widely identified in the Altun, Eastern Kunlun, and Qilian Mountains (Dong et al., 2021). The 180–300 Ma group of detrital zircon may be linked with Paleo-Tethys subduction-collision events in this region (Dong et al., 2021). The possible low-angle, north-dipping (current direction) subduction of the Paleo-Tethys resulted in magmatic events from 290 to 230 Ma in the southern Qilian-North Qaidam areas (Jian et al., 2020, 2024; Zhang et al., 2020). The detrital muscovite records are thought to be associated with the post-collisional

thermal relaxation after the closure of the back-arc basin (Zhou et al., 2022). Therefore a detrital zircon age group may be commonly followed by a detrital muscovite age group. The 300–450 Ma group of detrital muscovite grains in the Qaidam basin corresponds to the widespread 360–540 Ma group of detrital zircons. However, the detrital muscovite age data indicate <250 Ma muscovite grains are almost absent in the northern Qaidam basin and are minor in some analyzed samples from the western Qaidam basin (Fig. 12). The decoupling between Triassic–Permian zircon U-Pb ages and muscovite $^{40}\text{Ar}/^{39}\text{Ar}$ ages might be due to low muscovite fertility of the Triassic–Permian geological records (including magmatic, metamorphic and sedimentary records). The detrital apatite age records in the Cenozoic Qaidam basin may related to the late Mesozoic–Cenozoic uplift history, which is associated with the far-field effects of the Lhasa-Qiangtang and India-Asian collision (Jian et al., 2018; Kapp and DeCelles, 2019). The spatially varied detrital AFT age distributions indicate asynchronous uplift of surrounding mountain ranges or variable source terranes of the Qaidam basin, which may help in understanding the uplifting mechanism of the Tibetan Plateau.

It is worth noting that detrital zircon and apatite age spectra exhibit higher spatial variations compared to detrital muscovite records

(Figs. 10 and 11). This is likely due to the distinct source-to-sink behaviors of these detrital grains. Zircon and apatite are common granular heavy minerals in sandy sediments and sandstones, whereas muscovite is a platy light mineral in relatively fine-grained sediments and sedimentary rocks (e.g., silty or fine sandstones; Fig. 2). The different shapes of detrital muscovite, zircon, and apatite likely play a crucial role in causing the varied age distribution (Malusà and Garzanti, 2019). With their granular shape, detrital zircon and apatite are mainly transported by bed loads, whereas detrital muscovite is mainly transported by a suspended load (Fig. 13; Malusà and Garzanti, 2019). We infer that detrital muscovite grains from different source terranes may be transported over longer distances and mixed more thoroughly than detrital zircons and apatites, resulting in a relatively low age distribution variability (Fig. 13). In addition to transport and depositional processes, the tectonic history, parent rock types, and mineral fertility also significantly influence the age distributions of detrital minerals from the source end (Chew et al., 2020; Malusà and Garzanti, 2019; Malusà et al., 2016; Moecher and Samson, 2006). Muscovite is a common constituent of various lithologies, such as metasediments, and granite, and forms over a large pressure-temperature range (Stuart, 2002). Zircon is widely found in magmatic and metamorphic rocks, especially intermediate to Si-saturated magmatic rocks (Hoskin and Schaltegger, 2003; Chew et al., 2020). Apatite is a common accessory mineral in magmatic and metamorphic rocks (Chew et al., 2020). These three minerals are also prevalent in clastic sedimentary rocks (Chew et al., 2020; Stuart, 2002). This indicates that the rock types of source terranes and potential recycling should be carefully considered while using detrital multi-dating for provenance analyses. Furthermore, deep-burial processes could reset the age of detrital minerals with lower closure temperatures (e.g., apatite) as the depth of burial increases (Jian et al., 2018; Stockli and Najman, 2020).

5.4. The role of detrital muscovite records in revealing tectonic settings and provenance: A brief discussion

Detrital zircon U-Pb age distributions are considered a promising proxy for revealing tectonic settings of sedimentary basins, primarily based on the relationships between zircon crystallization ages and sediment depositional ages (Cawood et al., 2012; Sun et al., 2023). Since muscovite $^{40}\text{Ar}/^{39}\text{Ar}$ ages document the time when rocks cooled through closure temperatures of ca. 350–400 °C (Hodges et al., 2005; Stuart, 2002), detrital muscovite age spectra of sedimentary rocks are related to regional exhumation rates, which are likely controlled by tectonic settings and climate (Bermúdez et al., 2013; Burbank, 2018; DeCelles and Carrapa, 2023; Georgieva et al., 2016; Pundir et al., 2021; Sobel and Strecker, 2003; Thiede et al., 2004). However, the response of detrital muscovite $^{40}\text{Ar}/^{39}\text{Ar}$ ages to tectonic settings remains rarely reported, and the potential of detrital muscovite records reflecting tectonic attributes remains unclear. We recognized that the selection of the age model for the Qaidam basin may impact inter-basin comparisons. The Cenozoic Qaidam basin was considered a continental superimposed basin (Yin et al., 2008; Cheng et al., 2021) and its tectonic settings are thought to have not significantly varied since the onset of the Cenozoic deposition. Thus, all the Cenozoic Qaidam basin detrital muscovite age data are combined as a unit for the inter-basin comparisons, rather than using higher stratigraphic resolutions. The collected detrital muscovite $^{40}\text{Ar}/^{39}\text{Ar}$ data from the worldwide Cenozoic sedimentary basins show that syndepositional detrital muscovite grains are widely present in collision and convergence tectonic settings but absent in intracratonic tectonic settings (Fig. 14; e.g., Benowitz et al., 2019; Carrapa et al., 2009; Liu et al., 2020; Najman et al., 2009; Rahman and Faupl, 2003; Rieser et al., 2007; Stickroth et al., 2019; Uddin et al., 2010). Theoretically, under collision and convergence tectonic settings, source terranes around sedimentary basins may have higher exhumation rates,

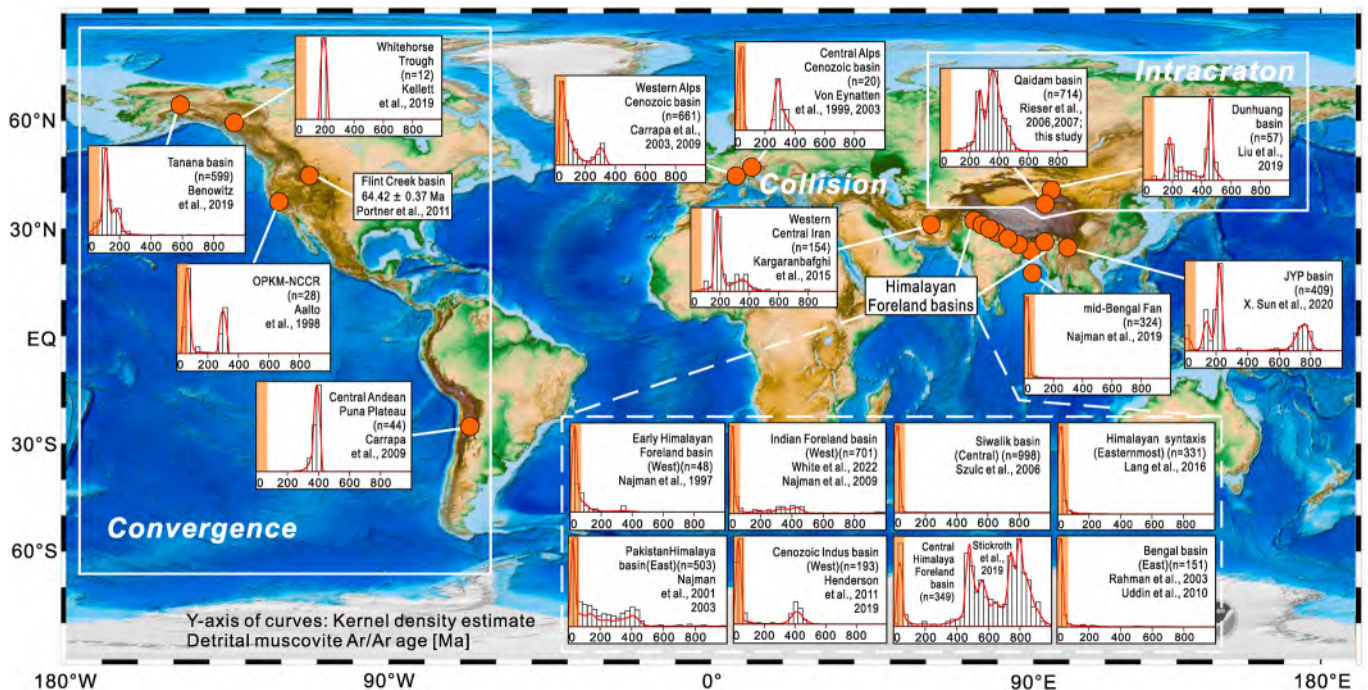


Fig. 14. Published detrital muscovite $^{40}\text{Ar}/^{39}\text{Ar}$ age studies, KDE curves, and histograms for the detrital muscovite $^{40}\text{Ar}/^{39}\text{Ar}$ age data of global Cenozoic sedimentary basins. The orange band marks the time frame of the Cenozoic Era. OPKM-NCCR: Olympic Peninsula, Klamath Mountains, and northern California Coast Ranges; JYB basins, Jianchuan and Yuanmou basins. Data are from Aalto et al. (1998); Benowitz et al. (2019); Carrapa et al. (2003, 2016, 2009); Henderson et al. (2010, 2011); Kargarabafghi et al. (2015); Kellett and Muniz (2019); Lang et al. (2016); Liu et al. (2020); Najman et al. (1997, 2001, 2003, 2009, 2019); Portner et al. (2011); Rahman and Faupl (2003); Rieser et al. (2006a, 2006b, 2007, 2010); Stickroth et al. (2019); Sun et al. (2020); Szulc et al. (2006); Uddin et al. (2010); von Eynatten et al. (1999); von Eynatten and Wijbrans (2003); White et al. (2002). The R programming language-based Provenance software (Vermeesch et al., 2016) was employed for the illustrations.

generating syndepositional detrital muscovite grains and $^{40}\text{Ar}/^{39}\text{Ar}$ ages close to depositional ages. The relatively older ages which are either prominent or subordinate (Fig. 14), are likely due to early stages of orogenic processes or preceding tectonic cycles. In intracratonic tectonic settings, source terranes with low exhumation rates during the last sedimentary cycle may only generate detrital muscovite grains with older age (Fig. 14). This is reinforced by the available detrital muscovite data from modern river sediments (Fig. 15). Detrital muscovite grains in sediments from rivers draining intracratonic regions show a large number of older ages (Fig. 15), whereas sediments from the rivers with collision and convergence backgrounds have a high abundance of detrital muscovite grains with ages close to the present time (Fig. 15). Several studies have highlighted that detrital muscovite $^{40}\text{Ar}/^{39}\text{Ar}$ ages may also be controlled by climate-induced exhumation processes in source terranes (Carrapa et al., 2014; Clift, 2017; Clift et al., 2008; Rieser et al., 2010). For example, the detrital muscovite age spectrum of the Pamir drainages is characterized by a dominant younger age group with a minor older age group (Fig. 15). The detrital muscovite age signatures of the rivers draining in the central and southern Pamir, where greater precipitation and higher-magnitude exhumation prevail, are characterized by younger ages than those from the northeastern Pamir (Fig. 15; Carrapa et al., 2014). This means that a more humid climate may lead to higher-magnitude exhumation, generating muscovite grains of younger ages that existed deep under the orogenic belts.

We consider that detrital muscovite $^{40}\text{Ar}/^{39}\text{Ar}$ age data hold significant promise for addressing various issues in geoscience. However, publications referring to detrital muscovite (or white mica) are far fewer than those referring to detrital zircon and apatite in the past decades (Fig. S3 in Appendix B). Several reasons may account for this discrepancy: 1) Mineral occurrence. Muscovite is a common constituent of metasedimentary rocks and granite as an accessory mineral or a main mineral phase, but zircon occurs in a wider range of rock types (Mark et al., 2016; Spiegel et al., 2004). 2) Transport and deposition. Detrital muscovite grains are generally transported by suspended load (Fig. 13; Malusà and Garzanti, 2019) and tend to be deposited along with other

very fine-grained, light grains (e.g., silt and mud detritus) in relatively low-energy sedimentary environments (Jirí, 2009; Stuart, 2002). Consequently, compared with zircon and apatite, muscovite is not a regular target for tracing sand (or sandstone) provenance. 3) Closure temperature. The moderate closure temperature of the muscovite $^{40}\text{Ar}/^{39}\text{Ar}$ system makes this dating technique mainly useful for addressing exhumation processes at 8–10 km depths for source terranes (Stuart, 2002). In contrast, the high closure temperatures for U-Pb isotopic systems and the low closure temperatures for fission track and (U-Th)/He systems make detrital zircon and apatite dating applicable to a broader range of issues, such as revealing tectonic-magmatic evolution related to plate tectonics and neotectonic events related to geological hazards (Cawood et al., 2012; Stockli and Najman, 2020). Additionally, in-situ zircon and apatite elemental and isotopic analysis techniques are widely used to unravel the petrogenesis of magmatic rocks (Bruand et al., 2017; Sun et al., 2010). 4) Technical complexity and cost. The in-situ single-grain $^{40}\text{Ar}/^{39}\text{Ar}$ analysis technique is expensive and requires complex, time-consuming operations.

5.5. Implications

Despite the above-mentioned limitations, detrital muscovite $^{40}\text{Ar}/^{39}\text{Ar}$ dating studies are still beneficial for understanding geological processes in sedimentary source terranes and play a crucial role in ascertaining fine-grained (e.g., muds and silts) sediment source-to-sink systems in some cases. Detrital muscovite grains are commonly present in the loess of the Chinese Loess Plateau (Jeong et al., 2017, Fig. 1A), which is considered to be formed by aeolian transport and mainly comprise silt grains (Pullen et al., 2011; Liu et al., 2016). Understanding loess provenance is fundamental to reconstructing wind patterns during the late Cenozoic (Sun, 2002; Pullen et al., 2011; Wang et al., 2020). Detrital zircon records have been extensively used to unravel the provenance of the Chinese Loess Plateau. Most studies indicate that the Qaidam basin is an important sediment source for the Chinese Loess Plateau (Pullen et al., 2011; Wang et al., 2020). Previous studies

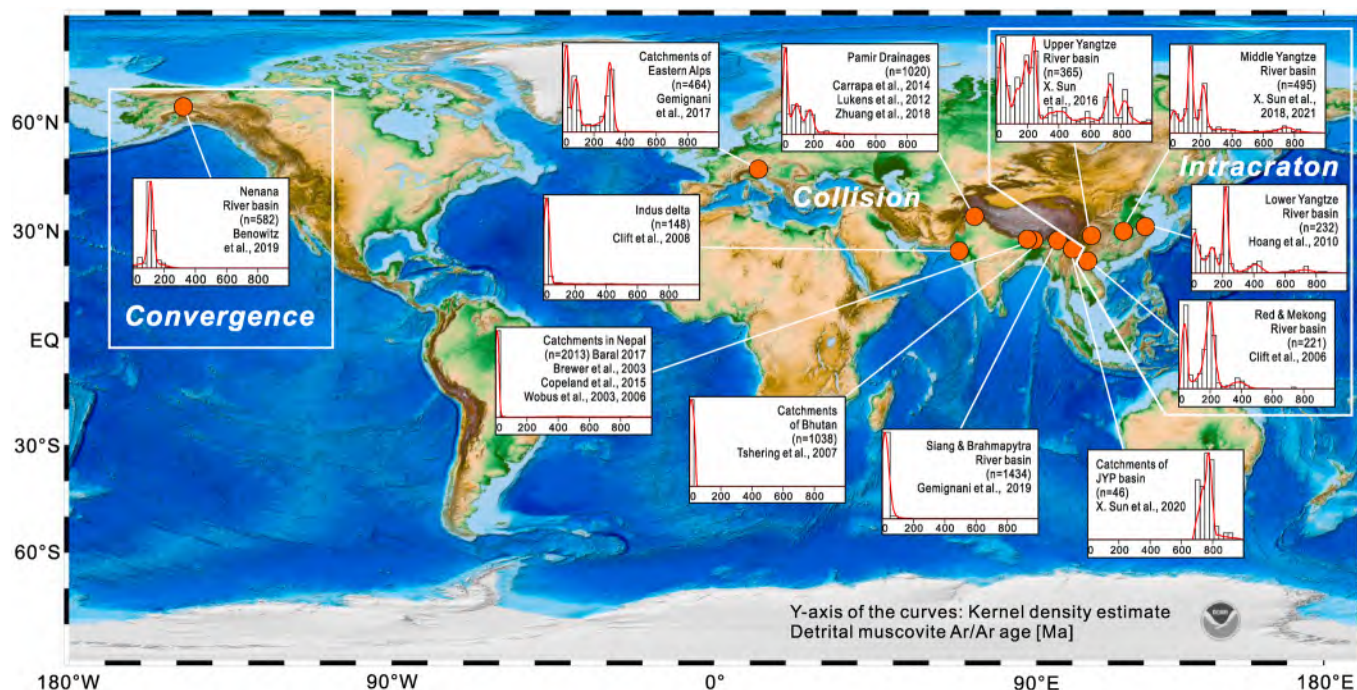


Fig. 15. Published detrital muscovite $^{40}\text{Ar}/^{39}\text{Ar}$ age studies, KDE curves, and histograms for the detrital muscovite $^{40}\text{Ar}/^{39}\text{Ar}$ age data of global modern river basins. JYB basins, Jianchuan and Yuanmou basins. Data are from Baral (2017); Benowitz et al. (2019); Brewer et al. (2003); Carrapa et al. (2014); Clift et al. (2006, 2008); Copeland et al. (2015); Gemignani et al. (2017, 2019); Lukens et al. (2012); Sun et al. (2020, 2016, 2018, 2021); Tshering (2007); Van Hoang et al. (2010); Wobus et al. (2003, 2006); Zhuang et al. (2018). The R programming language-based Provenance software (Vermeesch et al., 2016) was employed for the illustrations.

suggest that detrital zircon U-Pb age populations in the Cenozoic Qaidam basin were spatiotemporally diverse (Fig. 10; Jian et al., 2024). However, our findings indicate that detrital muscovite $^{40}\text{Ar}/^{39}\text{Ar}$ age ranges in the Cenozoic Qaidam basin are spatially similar (Fig. 6). The relatively well-mixed detrital muscovite $^{40}\text{Ar}/^{39}\text{Ar}$ age signals from the Qaidam basin (as source signals) suggest a high potential of the $^{40}\text{Ar}/^{39}\text{Ar}$ dating technique in Asian dust provenance studies.

6. Conclusions

Our new detrital muscovite $^{40}\text{Ar}/^{39}\text{Ar}$ dating results, combined with previously reported data, indicate that most Cenozoic deposits from the Qaidam basin have spatially similar detrital muscovite $^{40}\text{Ar}/^{39}\text{Ar}$ age ranges. These ages are predominantly 300–400 Ma, with subordinate ranges of 200–300 Ma and 400–500 Ma. This suggests that detrital muscovite records and corresponding provenance signals for the Cenozoic Qaidam basin are well-mixing spatially. However, the available data demonstrate that the Cenozoic deposits exhibit stratigraphically variable detrital muscovite $^{40}\text{Ar}/^{39}\text{Ar}$ age populations. This variability may be attributed to changes in sedimentary environments over time. Additionally, samples (host clastic rocks) with coarser grain sizes may have narrower detrital muscovite age ranges compared to samples with finer grain sizes. Therefore, it is important to consider natural biases from the source-to-sink systems, such as variations in sedimentary environments and grain sizes, when using the detrital single-grain dating technique for provenance interpretations.

A comparison of detrital muscovite, zircon, and apatite records from the Cenozoic Qaidam basin reveals that the detrital zircon U-Pb age spectra exhibit the oldest ages, the widest age ranges, and the largest number of age groups. Moreover, detrital zircon and apatite age spectra show higher spatial variation compared to detrital muscovite records. These differences can be explained by the distinct source-to-sink behaviors of detrital minerals. The magmatic or high-grade metamorphic history and high closure temperature of the zircon U-Pb system originally determined the oldest ages. The uplift history and relatively low closure temperature of muscovite $^{40}\text{Ar}/^{39}\text{Ar}$ and AFT systems result in relatively young age records. Parent rock types, mineral fertility, and weathering resistance control the numbers and distribution of the detrital age clusters. Additionally, the shape, density, and transport, depositional processes of minerals (i.e., different transport loads of light, platy minerals, and heavy, granular minerals) contribute to the variation in the age spectra.

The global compilation of detrital muscovite $^{40}\text{Ar}/^{39}\text{Ar}$ age data reveals that detrital muscovite $^{40}\text{Ar}/^{39}\text{Ar}$ geochronology has potentials to indicate tectonic settings. However, it is crucial to distinguish climatic signals before tectonic interpretation.

CRedit authorship contribution statement

Shuhuai Ye: Writing – review & editing, Writing – original draft, Investigation, Data curation, Conceptualization. **Xing Jian:** Writing – review & editing, Supervision, Resources, Funding acquisition, Data curation, Conceptualization. **Ling Fu:** Resources, Investigation. **Wei Zhang:** Writing – review & editing, Resources, Project administration. **Xiaotian Shen:** Writing – review & editing, Formal analysis. **Ping Guan:** Resources, Investigation.

Declaration of competing interest

The authors declare that they have no known competing financial interests or personal relationships that could have appeared to influence the work reported in this paper.

Data availability

I have shared the link to my data at the Attach file step.

Acknowledgments

This research was supported by the Natural Science Foundation of Xiamen, China (No. 35022Z0227006) and the Xiamen University Fundamental Research Funds for the Central Universities (Nos. 20720192011, 20720160114). We appreciate the consistent support from the PetroChina Qinghai Oilfield Company during borehole sample collection. Jianqing Ji and Jing Zhou from Peking University are appreciated for their help during the Ar-Ar dating analysis.

Appendix A. Supplementary data

Supplementary data to this article can be found online at <https://doi.org/10.1016/j.marpetgeo.2024.107068>.

References

- Aalto, K., Sharp, W., Renne, P., 1998. $^{40}\text{Ar}/^{39}\text{Ar}$ dating of detrital micas from Oligocene-Pleistocene sandstones of the Olympic Peninsula, Klamath Mountains, and northern California Coast Ranges: provenance and paleodrainage patterns. *Can. J. Earth Sci.* 35 (7), 735–745.
- Allen, M.B., Song, S., Wang, C., Zeng, R., Wen, T., 2023. An oblique subduction model for closure of the Proto-Tethys and Palaeo-Tethys oceans and creation of the Central China Orogenic Belt. *Earth Sci. Rev.* 104385 <https://doi.org/10.1016/j.earscirev.2023.104385>.
- Andersen, T., 2005. Detrital zircons as tracers of sedimentary provenance: limiting conditions from statistics and numerical simulation. *Chem. Geol.* 216 (3–4), 249–270. <https://doi.org/10.1016/j.chemgeo.2004.11.013>.
- Bao, J., Song, C., Yang, Y., Fang, X., Meng, Q., Feng, Y., He, P., 2019. Reduced chemical weathering intensity in the Qaidam Basin (NE Tibetan plateau) during the late Cenozoic. *J. Asian Earth Sci.* 170, 155–165. <https://doi.org/10.1016/j.jseas.2018.10.018>.
- Bao, J., Wang, Y., Song, C., Feng, Y., Hu, C., Zhong, S., Yang, J., 2017. Cenozoic sediment flux in the Qaidam Basin, northern Tibetan Plateau, and implications with regional tectonics and climate. *Global Planet. Change* 155, 56–69. <https://doi.org/10.1016/j.gloplacha.2017.03.006>.
- Baral, S., 2017. $^{40}\text{Ar}/^{39}\text{Ar}$ Dating of Detrital Muscovites from Sun-Koshi-Arun River Basin and Effect of Tectonics and Climate in the Eastern Himalayas (Doctoral Dissertation).
- Benowitz, J.A., Davis, K., Roeske, S., 2019. A river runs through it both ways across time: $^{40}\text{Ar}/^{39}\text{Ar}$ detrital and bedrock muscovite geochronology constraints on the Neogene paleodrainage history of the Nenana River system, Alaska Range. *Geosphere* 15 (3), 682–701. <https://doi.org/10.1130/ges01673.1>.
- Bermúdez, M.A., van der Beek, P.A., Bernet, M., 2013. Strong tectonic and weak climatic control on exhumation rates in the Venezuelan Andes. *Lithosphere* 5 (1), 3–16. <https://doi.org/10.1130/L212.1>.
- Bontje, C., 2015. PT History and $^{40}\text{Ar}/^{39}\text{Ar}$ Dating of the Jinshikou Group, Eastern Kunlun Mountains, Qinghai, China.
- Brewer, I.D., Burbank, D.W., Hodges, K.V., 2003. Modelling detrital cooling-age populations: insights from two Himalayan catchments. *Basin Res.* 15 (3), 305–320. <https://doi.org/10.1046/j.1365-2117.2003.00211.x>.
- Bruand, E., Fowler, M., Storey, C., Darling, J., 2017. Apatite trace element and isotope applications to petrogenesis and provenance. *Am. Mineral.* 102 (1), 75–84. <https://doi.org/10.2138/am-2017-5744>.
- Burbank, D.W., 2018. Rates of erosion and their implications for exhumation. *Mineral. Mag.* 66 (1), 25–52. <https://doi.org/10.1180/0026461026610014>.
- Bush, M.A., Saylor, J.E., Horton, B.K., Nie, J., 2016. Growth of the Qaidam Basin during Cenozoic exhumation in the northern Tibetan Plateau: inferences from depositional patterns and multiproxy detrital provenance signatures. *Lithosphere* 8 (1), 58–82. <https://doi.org/10.1130/L449.1>.
- Caracciolo, L., Critelli, S., Cavazza, W., Meinhold, G., von Eynatten, H., Manetti, P., 2015. The Rhodope Zone as a primary sediment source of the southern Thrace basin (NE Greece and NW Turkey): evidence from detrital heavy minerals and implications for central-eastern Mediterranean palaeogeography. *Int. J. Earth Sci.* 104 (3), 815–832. <https://doi.org/10.1007/s00531-014-1111-9>.
- Carrapa, B., 2010. Resolving tectonic problems by dating detrital minerals. *Geology* 38 (2), 191–192. <https://doi.org/10.1130/focus022010.1>.
- Carrapa, B., DeCelles, P.G., Reiners, P.W., Gehrels, G.E., Sudo, M., 2009. Apatite triple dating and white mica $^{40}\text{Ar}/^{39}\text{Ar}$ thermochronology of syntectonic detritus in the Central Andes: a multiphase tectonothermal history. *Geology* 37 (5), 407–410. <https://doi.org/10.1130/g25698a.1>.
- Carrapa, B., Di Giulio, A., Mancin, N., Stockli, D., Fantoni, R., Hughes, A., Gupta, S., 2016. Tectonic significance of Cenozoic exhumation and foreland basin evolution in the Western Alps. *Tectonics* 35 (8), 1892–1912. <https://doi.org/10.1002/2016tc004132>.
- Carrapa, B., Mustapha, F.S., Cosca, M., Gehrels, G., Schoenbohm, L.M., Sobel, E.R., DeCelles, P.G., Russell, J., Goodman, P., 2014. Multisystem dating of modern river detritus from Tajikistan and China: implications for crustal evolution and exhumation of the Pamir. *Lithosphere* 6 (6), 443–455. <https://doi.org/10.1130/L360.1>.

- Carrapa, B., Wijbrans, J., Bertotti, G., 2003. Episodic exhumation in the western alps. *Geology* 31 (7), 601–604. [https://doi.org/10.1130/0091-7613\(2003\)031<0601: Eeitwa>2.0.Co;2](https://doi.org/10.1130/0091-7613(2003)031<0601: Eeitwa>2.0.Co;2).
- Cawood, P.A., Hawkesworth, C.J., Dhuime, B., 2012. Detrital zircon record and tectonic setting. *Geology* 40 (10), 875–878. <https://doi.org/10.1130/g32945.1>.
- Cawood, P.A., Nemchin, A.A., 2000. Provenance record of a rift basin: U/Pb ages of detrital zircons from the Perth Basin, Western Australia. *Sediment. Geol.* 134 (3), 209–234. [https://doi.org/10.1016/S0037-0738\(00\)00044-0](https://doi.org/10.1016/S0037-0738(00)00044-0).
- Chamberlain, K.R., Bowring, S.A., 2001. Apatite–feldspar U–Pb thermochronometer: a reliable, mid-range (~450°C), diffusion-controlled system. *Chem. Geol.* 172 (1), 173–200. [https://doi.org/10.1016/S0009-2541\(00\)00242-4](https://doi.org/10.1016/S0009-2541(00)00242-4).
- Chen, L., Song, C., Wang, Y., Fang, X., Zhang, Y., Zhang, J., Chen, Y., He, P., 2021. Mesozoic–Cenozoic uplift/exhumation history of the Qilian Shan, NE Tibetan plateau: constraints from low-temperature thermochronology. *Front. Earth Sci.* 9 <https://doi.org/10.3389/feart.2021.760100>.
- Chen, N., Sun, M., He, L., Zhang, K., Wang, G., 2002. Precise timing of the early paleozoic metamorphism and thrust deformation in the eastern Kunlun orogen. *Chin. Sci. Bull.* 47, 1130–1133. <https://doi.org/10.1360/02tb9253>.
- Chen, W., Zhang, Y., Ji, Q., Wang, S., Zhang, J., 2002. Magmatism and deformation times of the Xidatan rock series, East Kunlun mountains. *Sci. China, Ser. B: Chem.* 45, 20–27. <https://doi.org/10.1007/BF02932203>.
- Chang, H., Li, L., Qiang, X., Garzzone, C.N., Pullen, A., An, Z., 2015. Magnetostratigraphy of Cenozoic deposits in the western Qaidam Basin and its implication for the surface uplift of the northeastern margin of the Tibetan Plateau. *Earth Planet. Sci. Lett.* 430, 271–283. <https://doi.org/10.1016/j.epsl.2015.08.029>.
- Chen, Y., Pei, X., Li, Z., Li, R., Liu, C., Wang, M., 2017. Magmatic events recorded in granitic gneisses from the Hatu area, eastern East Kunlun Orogen: response to the assembly of Rodinia. *Geol. J.* 52, 403–418. <https://doi.org/10.1002/gj.3006>.
- Cheng, F., Fu, S., Jolivet, M., Zhang, C., Guo, Z., 2015. Source to Sink Relation between the Eastern Kunlun Range and the Qaidam Basin, Northern Tibetan Plateau, during the Cenozoic. *Geological Society of America Bulletin*. <https://doi.org/10.1130/b31260.1>.
- Cheng, F., Garzzone, C.N., Jolivet, M., Guo, Z., Zhang, D., Zhang, C., Zhang, Q., 2019a. Initial deformation of the northern Tibetan plateau: insights from deposition of the Lulehe Formation in the Qaidam Basin. *Tectonics* 38 (2), 741–766. <https://doi.org/10.1029/2018tc005214>.
- Cheng, F., Garzzone, C.N., Mitra, G., Jolivet, M., Guo, Z., Lu, H., Li, X., Zhang, B., Zhang, C., Zhang, H., Wang, L., 2019b. The interplay between climate and tectonics during the upward and outward growth of the Qilian Shan orogenic wedge, northern Tibetan Plateau. *Earth Sci. Rev.* 198 <https://doi.org/10.1016/j.earscirev.2019.102945>.
- Cheng, F., Garzzone, C., Jolivet, M., Guo, Z., Zhang, D., Zhang, C., 2018. A new sediment accumulation model of Cenozoic depositional ages from the Qaidam Basin, Tibetan plateau. *J. Geophys. Res.: Earth Surf.* 123 (11), 3101–3121. <https://doi.org/10.1029/2018JF004645>.
- Cheng, F., Jolivet, M., Fu, S., Zhang, C., Zhang, Q., Guo, Z., 2016. Large-scale displacement along the Altyn Tagh fault (north Tibet) since its Eocene initiation: insight from detrital zircon U–Pb geochronology and subsurface data. *Tectonophysics* 677–678, 261–279. <https://doi.org/10.1016/j.tecto.2016.04.023>.
- Cheng, F., Jolivet, M., Guo, Z., Wang, L., Zhang, C., Li, X., 2021. Cenozoic evolution of the Qaidam basin and implications for the growth of the northern Tibetan plateau: a review. *Earth Sci. Rev.* 220 <https://doi.org/10.1016/j.earscirev.2021.103730>.
- Cheng, F., Zuza, A.V., Jolivet, M., Mulch, A., Meijer, N., Guo, Z., 2023. Linking source and sink: the timing of deposition of Paleogene syntectonic strata in Central Asia. *Geology* 51 (11), 1083–1088. <https://doi.org/10.1130/g51382.1>.
- Cherniak, D.J., Watson, E.B., 2001. Pb diffusion in zircon. *Chem. Geol.* 172 (1), 5–24. [https://doi.org/10.1016/S0009-2541\(00\)00233-3](https://doi.org/10.1016/S0009-2541(00)00233-3).
- Chew, D., O'Sullivan, G., Caracciolo, L., Mark, C., Tyrrell, S., 2020. Sourcing the sand: accessory mineral fertility, analytical and other biases in detrital U–Pb provenance analysis. *Earth Sci. Rev.* 202 <https://doi.org/10.1016/j.earscirev.2020.103093>.
- Clift, P.D., 2017. Cenozoic sedimentary records of climate–tectonic coupling in the Western Himalaya. *Prog. Earth Planet. Sci.* 4 (1) <https://doi.org/10.1186/s40645-017-0151-8>.
- Clift, P.D., Carter, A., Campbell, I.H., Pringle, M.S., Van Lap, N., Allen, C.M., Hodges, K.V., Tan, M.T., 2006. Thermochronology of mineral grains in the red and mekong rivers, vietnam: provenance and exhumation implications for southeast asia. *G-cubed* 7 (10). <https://doi.org/10.1029/2006gc001336> n/a-n/a.
- Clift, P.D., Giosan, L., Blusztajn, J., Campbell, I.H., Allen, C., Pringle, M., Tabrez, A.R., Danish, M., Rabbani, M.M., Alizai, A., Carter, A., Lückge, A., 2008. Holocene erosion of the Lesser Himalaya triggered by intensified summer monsoon. *Geology* 36 (1). <https://doi.org/10.1130/g24315a.1>.
- Copeland, P., 2020. On the use of geochronology of detrital grains in determining the time of deposition of clastic sedimentary strata. *Basin Res.* 32 (6), 1532–1546. <https://doi.org/10.1111/bre.12441>.
- Copeland, P., Bertrand, G., France-Lanord, C., Sundell, K., 2015. 40Ar/39Ar ages of muscovites from modern Himalayan rivers: himalayan evolution and the relative contribution of tectonics and climate. *Geosphere* 11 (6), 1837–1859. <https://doi.org/10.1130/ges01154.1>.
- Criniti, S., Martín-Martín, M., Martín-Algarra, A., 2023. New constraints for the western paleotethys paleogeography–paleotectonics derived from detrital signatures: malaguide carboniferous culm cycle (betic cordillera, S Spain). *Sediment. Geol.* 458, 106534 <https://doi.org/10.1016/j.sedgeo.2023.106534>.
- Criniti, S., Martín-Martín, M., Hlila, R., Maaté, A., Maaté, S., 2024. Detrital signatures of the ghomaride culm cycle (rif cordillera, N Morocco): new constraints for the northern gondwana plate tectonics. *Mar. Petrol. Geol.* 165, 106861 <https://doi.org/10.1016/j.marpetgeo.2024.106861>.
- Critelli, S., Criniti, S., 2021. Sandstone petrology and provenance in fold thrust belt and foreland basin system. In: Ali Ismail, A.-J. (Ed.), *Sedimentary Petrology*. IntechOpen. <https://doi.org/10.5772/intechopen.96985>. Ch. 1).
- Critelli, S., Martín-Martín, M., 2022. Provenance, paleogeographic and paleotectonic interpretations of Oligocene–Lower Miocene sandstones of the western-central Mediterranean region: a review. *J. Asian Earth Sci.* X 8, 100124. <https://doi.org/10.1016/j.jaesx.2022.100124>.
- Critelli, S., Martín-Martín, M., 2024. History of western Tethys Ocean and the birth of the circum-mediterranean orogeny as reflected by source-to-sink relations. *Int. Geol. Rev.* 66 (2), 505–515. <https://doi.org/10.1080/00206814.2023.2280787>.
- Critelli, S., Criniti, S., Ingersoll, R.V., Cavazza, W., 2023. Temporal and spatial significance of volcanic particles in sand(stone): implications for provenance and palaeotectonic reconstructions. In: Di Capua, A., De Rosa, R., Kereszturi, G., Le Pera, E., Rosi, M., Watt, S.F.L. (Eds.), *Volcanic Processes in the Sedimentary Record: when Volcanoes Meet the Environment*. Geological Society of London. <https://doi.org/10.1144/sp520-2022-99>.
- Critelli, S., Martín-Martín, M., Capobianco, W., Perri, F., 2021. Sedimentary history and palaeogeography of the cenozoic clastic wedges of the malaguide complex, internal betic cordillera, southern Spain. *Mar. Petrol. Geol.* 124, 104775 <https://doi.org/10.1016/j.marpetgeo.2020.104775>.
- Critelli, S., Perri, F., Arribas, J., Herrero, M.J., 2018. Sandstone detrital modes and diagenetic evolution of Mesozoic continental red beds from western-central circum-Mediterranean orogenic belts. In: Ingersoll, R.V., Lawton, T.F., Graham, S.A. (Eds.), *Tectonics, Sedimentary Basins, and Provenance: A Celebration of the Career of William R. Dickinson*, vol. 540. Geological Society of America. <https://doi.org/10.1130/2018.2540.06>.
- Dahl, P.S., 1997. A crystal-chemical basis for Pb retention and fission-track annealing systematics in U-bearing minerals, with implications for geochronology. *Earth Planet. Sci. Lett.* 150 (3), 277–290. [https://doi.org/10.1016/S0012-821X\(97\)00108-8](https://doi.org/10.1016/S0012-821X(97)00108-8).
- Dai, J., Wang, C., Hourigan, J., Santosh, M., 2013. Multi-stage tectono-magmatic events of the eastern Kunlun range, northern Tibet: insights from U–Pb geochronology and (U–Th)/He thermochronology. *Tectonophysics* 599, 97–106. <https://doi.org/10.1016/j.tecto.2013.04.005>.
- Danišik, M., Pfaff, K., Evans, N.J., Manoloukos, C., Staude, S., McDonald, B.J., Markl, G., 2010. Tectonothermal history of the Schwarzwald Ore District (Germany): an apatite triple dating approach. *Chem. Geol.* 278 (1–2), 58–69. <https://doi.org/10.1016/j.chemgeo.2010.08.022>.
- DeCelles, P.G., Carrapa, B., 2023. Differences between the central Andean and Himalayan orogenic wedges: a matter of climate. *Earth Planet. Sci. Lett.* 616 <https://doi.org/10.1016/j.epsl.2023.118216>.
- DeCelles, P.G., Gehrels, G.E., Najman, Y., Martin, A.J., Carter, A., Garzanti, E., 2004. Detrital geochronology and geochemistry of Cretaceous–Early Miocene strata of Nepal: implications for timing and diachroneity of initial Himalayan orogenesis. *Earth Planet. Sci. Lett.* 227 (3–4), 313–330. <https://doi.org/10.1016/j.epsl.2004.08.019>.
- Deino, A., 2010. *User Manual for Mass Spec V. 7.84*. Berkeley Geochronology Center Special Publication.
- Dickinson, W.R., Gehrels, G.E., 2008. U–Pb ages of detrital zircons in relation to paleogeography: Triassic paleodrainage networks and sediment dispersal across southwest Laurentia. *J. Sediment. Res.* 78 (12), 745–764. <https://doi.org/10.2110/jsr.2008.088>.
- Dickinson, W.R., Gehrels, G.E., 2009a. U–Pb ages of detrital zircons in Jurassic eolian and associated sandstones of the Colorado Plateau: evidence for transcontinental dispersal and intraregional recycling of sediment. *Geol. Soc. Am. Bull.* 121 (3–4), 408–433. <https://doi.org/10.1130/b26406.1>.
- Dickinson, W.R., Gehrels, G.E., 2009b. Use of U–Pb ages of detrital zircons to infer maximum depositional ages of strata: a test against a Colorado Plateau Mesozoic database. *Earth Planet. Sci. Lett.* 288 (1–2), 115–125.
- Dickinson, W.R., Lawton, T.F., Gehrels, G.E., 2009. Recycling detrital zircons: a case study from the Cretaceous Bisbee Group of southern Arizona. *Geology* 37 (6), 503–506.
- Ding, X., Fu, L., Guan, P., Zhang, D., 2022. The southwestern boundary of Cenozoic Qaidam Basin: constraints from heavy mineral analysis. *Minerals* 12 (6). <https://doi.org/10.3390/min12060768>.
- Dong, Y., Sun, S., Santosh, M., Zhao, J., Sun, J., He, D., Shi, X., Hui, B., Cheng, C., Zhang, W., 2021. Central China orogenic belt and amalgamation of East Asian continents. *Gondwana Res.* 100, 131–194. <https://doi.org/10.1016/j.gr.2021.03.006>.
- Du, D.-d., Zhang, C.-j., Mughal, M.S., Wang, X.-y., Blaise, D., Gao, J.-p., Ma, Y., Luo, X.-r., 2018. Detrital apatite fission track constraints on Cenozoic tectonic evolution of the northeastern qinghai-tibet plateau, China: evidence from Cenozoic strata in Lulehe section, northern Qaidam Basin. *J. Mt. Sci.* 15 (3), 532–547. <https://doi.org/10.1007/s11629-017-4692-5>.
- Duan, L., Zhang, B., Wang, W., Zhang, P., Tang, Q., Chen, G., Jia, J., Yan, Y., Huang, R., Zheng, W., 2022. Magnetostratigraphy of the Cenozoic Lulehe section in the Qaidam Basin: implications for the tectonic deformation on the northeastern Tibetan plateau. *Chin. Sci. Bull.* 67, 872–887.
- Fang, J., Zhang, L., Chen, H., Zheng, Y., Li, D., Wang, C., Shen, D., 2018. Genesis of the Weibao banded skarn Pb–Zn deposit, Qimantagh, Xinjiang: insights from skarn mineralogy and muscovite 40Ar–39Ar dating. *Ore Geol. Rev.* 100, 483–503. <https://doi.org/10.1016/j.oregeorev.2017.06.001>.
- Fang, X., Galy, A., Yang, Y., Zhang, W., Ye, C., Song, C., 2019. Paleogene global cooling–induced temperature feedback on chemical weathering, as recorded in the northern Tibetan Plateau. *Geology* 47 (10), 992–996. <https://doi.org/10.1130/g46422.1>.

- Fang, X., Zhang, W., Meng, Q., Gao, J., Wang, X., King, J., Song, C., Dai, S., Miao, Y., 2007. High-resolution magnetostratigraphy of the neogene Huaitoutala section in the eastern Qaidam Basin on the NE Tibetan plateau, Qinghai province, China and its implication on tectonic uplift of the NE Tibetan plateau. *Earth Planet Sci. Lett.* 258 (1–2), 293–306. <https://doi.org/10.1016/j.epsl.2007.03.042>.
- Farley, K., 2000. Helium diffusion from apatite: general behavior as illustrated by Durango fluorapatite. *J. Geophys. Res. Solid Earth* 105 (B2), 2903–2914. <https://doi.org/10.1029/1999JB900348>.
- Feng, C., Li, G., Li, D., Zhou, A., Li, H., 2013. Ore-controlling structure and 40Ar/39Ar geochronology of Kekekaerde tungsten-tin deposit in Qimantage area, Xinjiang. *Miner. Deposits* 32 (1), 207–216 in Chinese with English abstract.
- Fildani, A., Weislogel, A., Drinkwater, N.J., McHargue, T., Tankard, A., Wooden, J., Hodgson, D., Flint, S., 2009. U-Pb zircon ages from the southwestern Karoo Basin, South Africa—implications for the Permian-Triassic boundary. *Geology* 37 (8), 719–722. <https://doi.org/10.1130/G25685A.1>.
- Fu, H., Jian, X., Liang, H., Zhang, W., Shen, X., Wang, L., 2022. Tectonic and climatic forcing of chemical weathering intensity in the northeastern Tibetan Plateau since the middle Miocene. *Catena* 208. <https://doi.org/10.1016/j.catena.2021.105785>.
- Gao, W., Wang, Z., Li, L., Qian, T., Cui, M., 2021. 40Ar/39Ar laser dating of the Zongwulong ductile shear zone in northeastern Tibetan Plateau: constraints on the time of Indosinian orogeny. *Chin. Geol.* 48 (1), 149–160 in Chinese with English abstract.
- Garzanti, E., 2016. From static to dynamic provenance analysis—sedimentary petrology upgraded. *Sediment. Geol.* 336, 3–13. <https://doi.org/10.1016/j.sedgeo.2015.07.010>.
- Gehrels, G., 2014. Detrital zircon U-Pb geochronology applied to tectonics. *Annu. Rev. Earth Planet Sci.* 42, 127–149. <https://doi.org/10.1146/annurev-earth-050212-124012>.
- Gehrels, G.E., Yin, A., Wang, X.F., 2003b. Magmatic history of the northeastern Tibetan Plateau. *J. Geophys. Res. Solid Earth* 108 (B9). <https://doi.org/10.1029/2002JB001876>.
- Gehrels, G.E., Yin, A., Wang, X.-F., 2003a. Detrital-zircon geochronology of the northeastern Tibetan plateau. *Geol. Soc. Am. Bull.* 115 (7), 881–896. [https://doi.org/10.1130/0016-7606\(2003\)115<0881:DGOTNT>2.0.CO;2](https://doi.org/10.1130/0016-7606(2003)115<0881:DGOTNT>2.0.CO;2).
- Gemignani, L., Kuiper, K.F., Wijbrans, J.R., Sun, X., Santato, A., 2019. Improving the precision of single grain mica 40Ar/39Ar-dating on smaller and younger muscovite grains: application to provenance studies. *Chem. Geol.* 511, 100–111. <https://doi.org/10.1016/j.chemgeo.2019.02.013>.
- Gemignani, L., Sun, X., Braun, J., van Gerve, T.D., Wijbrans, J.R., 2017. A new detrital mica 40Ar/39Ar dating approach for provenance and exhumation of the Eastern Alps. *Tectonics* 36 (8), 1521–1537. <https://doi.org/10.1002/2017tc004483>.
- Genser, J., Liu, Y., Neubauer, F., Ren, S., 2010. Ar-Ar ages of detrital mica from rivers draining the Qilian Shan on the NW margin of the Qaidam basin. *Terra. Nova* 18, 79–87.
- Georgieva, V., Melnick, D., Schildgen, T.F., Ehlers, T.A., Lagabrielle, Y., Enkelmann, E., Strecker, M.R., 2016. Tectonic control on rock uplift, exhumation, and topography above an oceanic ridge collision: southern Patagonian Andes (47°S), Chile. *Tectonics* 35 (6), 1317–1341. <https://doi.org/10.1002/2016tc004120>.
- Green, P., Duddy, I., Laslett, G., Hegarty, K., Gleadow, A.W., Lovering, J., 1989. Thermal annealing of fission tracks in apatite 4. Quantitative modelling techniques and extension to geological timescales. *Chem. Geol. Isot. Geosci.* 79 (2), 155–182. [https://doi.org/10.1016/0168-9622\(89\)90018-3](https://doi.org/10.1016/0168-9622(89)90018-3).
- Guo, T., Tan, S., Chang, G., Ding, Y., Zhang, Z., 2012. 40Ar/39Ar dating of the muscovite in the sericitic of the qimantage ductile shear zone and its geological significance. *Northwest. Geol.* 45 (1), 94–101 in Chinese with English abstract.
- Guo, P., Liu, C., Huang, L., Wang, P., Wang, K., Yuan, H., Xu, C., Zhang, Y., 2017. Genesis of the late Eocene bedded halite in the Qaidam Basin and its implication for paleoclimate in East Asia. *Palaeogeogr. Palaeoclimatol. Palaeoecol.* 487, 364–380. <https://doi.org/10.1016/j.palaeo.2017.09.023>.
- Hames, W., Bowring, S., 1994. An empirical evaluation of the argon diffusion geometry in muscovite. *Earth Planet Sci. Lett.* 124 (1–4), 161–169. [https://doi.org/10.1016/0012-821X\(94\)00079-4](https://doi.org/10.1016/0012-821X(94)00079-4).
- He, P., Song, C., Wang, Y., Meng, Q., Chen, L., Yao, L., Huang, R., Feng, W., Chen, S., 2018. Cenozoic deformation history of the Qilian Shan (northeastern Tibetan Plateau) constrained by detrital apatite fission-track thermochronology in the northeastern Qaidam Basin. *Tectonophysics* 749, 1–11. <https://doi.org/10.1016/j.tecto.2018.10.017>.
- He, P., Song, C., Wang, Y., Meng, Q., Wang, D., Feng, Y., Chen, L., Feng, W., 2020. Early Cenozoic exhumation in the Qilian Shan, northeastern margin of the Tibetan Plateau: insights from detrital apatite fission track thermochronology. *Terra. Nova* 32 (6), 415–424. <https://doi.org/10.1111/ter.12478>.
- He, P., Song, C., Wang, Y., Wang, D., Chen, L., Meng, Q., Fang, X., 2021a. Early Cenozoic activated deformation in the Qilian Shan, northeastern Tibetan Plateau: insights from detrital apatite fission-track analysis. *Basin Res.* 33 (3), 1731–1748. <https://doi.org/10.1111/bre.12533>.
- He, P., Song, C., Wang, Y., Zhang, Y., Chen, W., Meng, Q., Zhao, Y., 2021b. Intensified late miocene deformation in the northern Qaidam Basin, northern Tibetan plateau, constrained by apatite fission-track thermochronology. *Front. Earth Sci.* 9. <https://doi.org/10.3389/feart.2021.750993>.
- Henderson, A.L., Najman, Y., Parrish, R., BouDagher-Fadel, M., Barford, D., Garzanti, E., Andó, S., 2010. Geology of the Cenozoic Indus Basin sedimentary rocks: paleoenvironmental interpretation of sedimentation from the western Himalaya during the early phases of the India-Eurasia collision. *Tectonics* 29 (6). <https://doi.org/10.1029/2009tc002651> n/a-n/a.
- Henderson, A.L., Najman, Y., Parrish, R., Mark, D.F., Foster, G.L., 2011. Constraints to the timing of India-Eurasia collision; a re-evaluation of evidence from the Indus basin sedimentary rocks of the Indus-Tsangpo suture zone, Ladakh, India. *Earth Sci. Rev.* 106 (3–4), 265–292. <https://doi.org/10.1016/j.earscirev.2011.02.006>.
- Hodges, K., Ruhl, K., Wobus, C., Pringle, M., 2005. 40Ar/39Ar thermochronology of detrital minerals. *Rev. Mineral. Geochem.* 58 (1), 239–257. <https://doi.org/10.2138/rmg.2005.58.9>.
- Hong, D., Jian, X., Fu, L., Zhang, W., 2020. Garnet trace element geochemistry as a sediment provenance indicator: an example from the Qaidam basin, northern Tibet. *Mar. Petrol. Geol.* 116. <https://doi.org/10.1016/j.marpetgeo.2020.104316>.
- Hoskin, P.W., Schaltegger, U., 2003. The composition of zircon and igneous and metamorphic petrogenesis. *Rev. Mineral. Geochem.* 53 (1), 27–62. <https://doi.org/10.2113/0530027>.
- Hu, R., Wijbrans, J.R., Brouwer, F.M., Wang, M., Zhao, L., Qiu, H., 2016. 40Ar/39Ar thermochronological constraints on the retrogression and exhumation of ultra-high pressure (UHP) metamorphic rocks from Xitieshan terrane, North Qaidam, China. *Gondwana Res.* 36, 157–175. <https://doi.org/10.1016/j.gr.2016.04.009>.
- Jeong, G.Y., Hillier, S., Kemp, R.A., 2017. Changes in mineralogy of loess-paleosol sections across the Chinese Loess Plateau. *Quaternary Research* 75 (1), 245–255. <https://doi.org/10.1016/j.yqres.2010.09.001>.
- Ji, J., Zhang, K., Clift, P.D., Zhuang, G., Song, B., Ke, X., Xu, Y., 2017. High-resolution magnetostratigraphic study of the paleogene-neogene strata in the northern Qaidam Basin: implications for the growth of the northeastern Tibetan plateau. *Gondwana Res.* 46, 141–155. <https://doi.org/10.1016/j.gr.2017.02.015>.
- Jian, X., Fu, L., Wang, P., Guan, P., Zhang, W., Fu, H., Mei, H., 2023. Sediment provenance of the Lulehe Formation in the Qaidam basin: insight to initial Cenozoic deposition and deformation in northern Tibetan plateau. *Basin Res.* <https://doi.org/10.1111/bre.12712>.
- Jian, X., Guan, P., Fu, L., Zhang, W., Shen, X., Fu, H., Wang, L., 2024. Detrital zircon geochronology and provenance of Cenozoic deposits in the Qaidam basin, northern Tibetan plateau: an overview with new data, implications and perspectives. *Mar. Petrol. Geol.* 159. <https://doi.org/10.1016/j.marpetgeo.2023.106566>.
- Jian, X., Guan, P., Fu, S.-T., Zhang, D.-W., Zhang, W., Zhang, Y.-S., 2014. Miocene sedimentary environment and climate change in the northwestern Qaidam basin, northeastern Tibetan Plateau: facies, biomarker and stable isotopic evidences. *Palaeogeogr. Palaeoclimatol. Palaeoecol.* 414, 320–331. <https://doi.org/10.1016/j.palaeo.2014.09.011>.
- Jian, X., Guan, P., Zhang, D.-W., Zhang, W., Feng, F., Liu, R.-J., Lin, S.-D., 2013a. Provenance of Tertiary sandstone in the northern Qaidam basin, northeastern Tibetan Plateau: integration of framework petrography, heavy mineral analysis and mineral chemistry. *Sediment. Geol.* 290, 109–125. <https://doi.org/10.1016/j.sedgeo.2013.03.010>.
- Jian, X., Guan, P., Zhang, W., Feng, F., 2013b. Geochemistry of Mesozoic and Cenozoic sediments in the northern Qaidam basin, northeastern Tibetan Plateau: implications for provenance and weathering. *Chem. Geol.* 360–361, 74–88. <https://doi.org/10.1016/j.chemgeo.2013.10.011>.
- Jian, X., Guan, P., Zhang, W., Liang, H., Feng, F., Fu, L., 2018. Late Cretaceous to early Eocene deformation in the northern Tibetan Plateau: detrital apatite fission track evidence from northern Qaidam basin. *Gondwana Res.* 60, 94–104. <https://doi.org/10.1016/j.gr.2018.04.007>.
- Jian, X., Weislogel, A., Pullen, A., Shang, F., 2020. Formation and evolution of the Eastern Kunlun Range, northern Tibet: evidence from detrital zircon U-Pb geochronology and Hf isotopes. *Gondwana Res.* 83, 63–79. <https://doi.org/10.1016/j.gr.2020.01.015>.
- Jirí, K., 2009. Phyllosilicates in the sediment-forming processes: weathering, erosion, transportation, and deposition/Jirí Kontak. *Acta Geodyn. Geomater.* 6 (1), 153.
- Kapp, P., DeCelles, P.G., 2019. Mesozoic–Cenozoic geological evolution of the Himalayan-Tibetan orogen and working tectonic hypotheses. *Am. J. Sci.* 319 (3), 159–254.
- Kargaranbafghi, F., Neubauer, F., Genser, J., 2015. The tectonic evolution of western Central Iran seen through detrital white mica. *Tectonophysics* 651–652, 138–151. <https://doi.org/10.1016/j.tecto.2015.03.019>.
- Kellett, D., Muniz, P.I., 2019. Detrital U-Pb zircon and 40Ar/39Ar muscovite geochronology of the whitehorse trough, and surrounding rocks, yukon and British Columbia. In: *Geological Survey of Canada, Open File*.
- Kirkland, C.L., Barham, M., Danišik, M., 2020. Find a match with triple-dating: antarctic sub-ice zircon detritus on the modern shore of Western Australia. *Earth Planet Sci. Lett.* 531. <https://doi.org/10.1016/j.epsl.2019.115953>.
- Lang, K.A., Huntington, K.W., Burmester, R., Housen, B., 2016. Rapid exhumation of the eastern Himalayan syntaxis since the late Miocene. *Geol. Soc. Am. Bull.* 128 (9–10), 1403–1422. <https://doi.org/10.1130/b31419.1>.
- Li, B., Zuba, A.V., Chen, X., Hu, D., Shao, Z., Qi, B., Wang, Z.-z., Levy, D.A., Xiong, X., 2020. Cenozoic multi-phase deformation in the Qilian Shan and out-of-sequence development of the northern Tibetan Plateau. *Tectonophysics* 782–783. <https://doi.org/10.1016/j.tecto.2020.228423>.
- Li, C., Zheng, D., Zhou, R., Wang, W., Yu, J., Liu, C., Wang, Y., Pang, J., Ma, Y., Hao, Y., Li, Y., Wang, X., 2021. Topographic growth of the northeastern Tibetan Plateau during the middle-late Miocene: insights from integrated provenance analysis in the NE Qaidam Basin. *Basin Res.* 33 (6), 3212–3230. <https://doi.org/10.1111/bre.12600>.
- Li, H., Wang, C., Hames, W., Hao, J., Meert, J.G., Yu, Z., Zhang, S., Sun, X., Ma, D., Li, X., 2022. Grenville-age basement and early paleozoic reworking in the qilian orogen, NW China: implications for paleotectonic reconstruction of Rodinia and gondwana. *J. Asian Earth Sci.* 237, 105351. <https://doi.org/10.1016/j.jseaes.2022.105351>.
- Li, X., 2022. Source-to-sink Responses to the Migration of Depocenters during Cenozoic in the Qaidam Basin (Master's Thesis. Jilin University. <https://link.cnki.net/doi/10.27405/d.cnki.gxbdu.2022.001412>).

- Li, Y., Xiang, H., Zheng, J., Qiu, H., Bai, X., Brouwer, F.M., 2022. Petrology and PTT path of huangyuan group and maxianshan group in the central qilian block, NW China: implications for tectonic evolution of the Proto-Tethys Ocean. *J. Petrol.* 63 (8), egac077 <https://doi.org/10.1093/petrology/egac077>.
- Lin, X., Tian, Y., Donelick, R.A., Liu-Zeng, J., Cleber, S.J., Li, C.a., Wu, Q., Li, Z., 2019. Mesozoic and Cenozoic tectonics of the northeastern edge of the Tibetan plateau: evidence from modern river detrital apatite fission-track age constraints. *J. Asian Earth Sci.* 170, 84–95. <https://doi.org/10.1016/j.jseas.2018.10.028>.
- Lin, Y., Zhang, L., 2012. Petrology and 40Ar/39Ar geochronology of lawsonite-bearing blueschist and eclogite from the qingshuigou blueschist belt in north qilian mountains in NW China and their implication. *Acta Geol. Sin.* 86 (9), 1503–1524 in Chinese with English abstract.
- Liu, Y., Genser, J., Ge, X., Neubauer, F., Friedl, G., Chang, L., Ren, S., Handler, R., 2003. 40 Ar/39 Ar age evidence for Altyn fault tectonic activities in western China. *Chin. Sci. Bull.* 48, 2024–2030. <https://doi.org/10.1007/BF03183998>.
- Liu, Y., Genser, J., Neubauer, F., Jin, W., Ge, X., Handler, R., Takasu, A., 2005. 40Ar/39Ar mineral ages from basement rocks in the Eastern Kunlun Mountains, NW China, and their tectonic implications. *Tectonophysics* 398 (3–4), 199–224. <https://doi.org/10.1016/j.tecto.2005.02.007>.
- Liu, Y., Ren, S., Liu, Y., Genser, J., Neubauer, F., 2020. Early pleistocene uplift of the northeastern Tibetan plateau: evidence from the dunhuang basin, NW China. *J. Asian Earth Sci.* 188 <https://doi.org/10.1016/j.jseas.2019.104130>.
- Liu, Y., Yang, Y., Song, B., Galy, A., Zhang, F., Jin, Z., Zhang, G., Ye, C., Fang, X., 2022. Hydrothermal systems with radiogenic Sr in the North Qaidam ultrahigh-pressure metamorphic belt, NE Tibetan Plateau and implications for regional dissolved Sr budget. *Appl. Geochem.* 138 <https://doi.org/10.1016/j.apgeochem.2022.105214>.
- Liu, Y., Yang, Y., Yang, R., Galy, A., Jin, Z., Fang, X., Song, B., 2023. Deciphering source-to-sink history from a solute perspective: a Sr isotope approach in the Qaidam Basin, NE Tibet. *Gondwana Res.* 118, 76–91. <https://doi.org/10.1016/j.gr.2023.02.012>.
- Liu, Y.-J., Neubauer, F., Genser, J., Ge, X.-H., Takasu, A., Yuan, S.-H., Chang, L.-H., Li, W.-M., 2007. Geochronology of the initiation and displacement of the Altyn strike-slip fault, western China. *J. Asian Earth Sci.* 29 (2–3), 243–252. <https://doi.org/10.1016/j.jseas.2006.03.002>.
- Liu, Z., Liu, F., Ma, F., Wang, M., Bai, X., Zheng, Y., Yin, H., Zhang, G., 2016. Collapsibility, composition, and microstructure of loess in China. *Can. Geotech. J.* 53 (4), 673–686. <https://doi.org/10.1139/cgj-2015-0285>.
- Lu, H., Malusà, M.G., Zhang, Z., Guo, L., Shi, X., Ye, J., Sang, S., Xiong, S., Pan, J., Li, H., 2022a. Syntectonic sediment recycling controls eolian deposition in eastern asia since ~8 Ma. *Geophys. Res. Lett.* 49 (3) <https://doi.org/10.1029/2021gl096789>.
- Lu, H., Sang, S., Wang, P., Zhang, Z., Pan, J., Li, H., 2022b. Initial uplift of the Qilian Shan, northern Tibet since ca. 25 Ma: implications for regional tectonics and origin of eolian deposition in Asia. *GSA Bulletin Geological Society of America Bulletin* 134 (9–10), 2531–2547. <https://doi.org/10.1130/b36242.1>.
- Lu, H., Ye, J., Guo, L., Pan, J., Xiong, S., Li, H., 2018. Towards a clarification of the provenance of Cenozoic sediments in the northern Qaidam Basin. *Lithosphere* 11 (2), 252–272. <https://doi.org/10.1130/l1037.1>.
- Lukens, C.E., Carrapa, B., Singer, B.S., Gehrels, G., 2012. Miocene exhumation of the Pamir revealed by detrital geochronology of Tajik rivers. *Tectonics* 31 (2). <https://doi.org/10.1029/2011tc003040> n/a-n/a.
- Malusà, M.G., Garzanti, E., 2019. The sedimentology of detrital thermochronology. In: *Fission-Track Thermochronology and its Application to Geology*, pp. 123–143. https://doi.org/10.1007/978-3-319-89421-8_7.
- Malusà, M.G., Carter, A., Limoncelli, M., Villa, I.M., Garzanti, E., 2013. Bias in detrital zircon geochronology and thermochronometry. *Chem. Geol.* 359, 90–107. <https://doi.org/10.1016/j.chemgeo.2013.09.016>.
- Malusà, M.G., Resentini, A., Garzanti, E., 2016. Hydraulic sorting and mineral fertility bias in detrital geochronology. *Gondwana Res.* 31, 1–19. <https://doi.org/10.1016/j.gr.2015.09.002>.
- Mark, C., Cogné, N., Chew, D., 2016. Tracking exhumation and drainage divide migration of the Western Alps: a test of the apatite U-Pb thermochronometer as a detrital provenance tool. *Geol. Soc. Am. Bull.* 128 (9–10), 1439–1460. <https://doi.org/10.1130/b31351.1>.
- McRivette, M.W., Yin, A., Chen, X., Gehrels, G.E., 2019. Cenozoic basin evolution of the central Tibetan plateau as constrained by U-Pb detrital zircon geochronology, sandstone petrology, and fission-track thermochronology. *Tectonophysics* 751, 150–179. <https://doi.org/10.1016/j.tecto.2018.12.015>.
- Mezger, K., Krogstad, E., 1997. Interpretation of discordant U–Pb zircon ages: an evaluation. *J. Metamorph. Geol.* 15 (1), 127–140. <https://doi.org/10.1111/j.1525-1314.1997.00008.x>.
- Moecher, D.P., Samson, S.D., 2006. Differential zircon fertility of source terranes and natural bias in the detrital zircon record: implications for sedimentary provenance analysis. *Earth Planet Sci. Lett.* 247 (3–4), 252–266. <https://doi.org/10.1016/j.epsl.2006.04.035>.
- Moecher, D.P., Kelly, E.A., Hietpas, J., Samson, S.D., 2019. Proof of recycling in clastic sedimentary systems from textural analysis and geochronology of detrital monazite: implications for detrital mineral provenance analysis. *GSA Bulletin Geological Society of America Bulletin* 131 (7–8), 1115–1132. <https://doi.org/10.1130/b31947.1>.
- Najman, Y., Bickle, M., Garzanti, E., Pringle, M., Barfod, D., Brozovic, N., Burbank, D., Ando, S., 2009. Reconstructing the exhumation history of the Lesser Himalaya, NW India, from a multitechnique provenance study of the foreland basin Siwalik Group. *Tectonics* 28 (5). <https://doi.org/10.1029/2009tc002506> n/a-n/a.
- Najman, Y., Garzanti, E., Pringle, M., Bickle, M., Stix, J., Khan, I., 2003. Early-middle miocene paleodrainage and tectonics in the Pakistan Himalaya. *Geol. Soc. Am. Bull.* 115 (10), 1265–1277. <https://doi.org/10.1130/B25165.1>.
- Najman, Y., Mark, C., Barfod, D.N., Carter, A., Parrish, R., Chew, D., Gemignani, L., 2019. Spatial and temporal trends in exhumation of the Eastern Himalaya and syntaxis as determined from a multitechnique detrital thermochronological study of the Bengal Fan. *GSA Bulletin Geological Society of America Bulletin* 131 (9–10), 1607–1622. <https://doi.org/10.1130/b35031.1>.
- Najman, Y., Pringle, M., Godin, L., Oliver, G., 2001. Dating of the oldest continental sediments from the Himalayan foreland basin. *Nature* 410 (6825), 194–197. <https://doi.org/10.1038/35065577>.
- Najman, Y., Pringle, M., Johnson, M., Robertson, A., Wijbrans, J., 1997. Laser 40Ar/39Ar dating of single detrital muscovite grains from Early foreland-basin sedimentary deposits in India: implications for early Himalayan evolution. *Geology* 25 (6), 535–538. [https://doi.org/10.1130/0091-7613\(1997\)025<0535:LAADOS>2.3.CO;2](https://doi.org/10.1130/0091-7613(1997)025<0535:LAADOS>2.3.CO;2).
- Nie, J., Ren, X., Saylor, J.E., Su, Q., Horton, B.K., Bush, M.A., Chen, W., Pfaff, K., 2019. Magnetic polarity stratigraphy, provenance, and paleoclimate analysis of Cenozoic strata in the Qaidam Basin, NE Tibetan Plateau. *GSA Bulletin Geological Society of America Bulletin* 132 (1–2), 310–320. <https://doi.org/10.1130/b35175.1>.
- Pang, J., Yu, J., Zheng, D., Wang, W., Ma, Y., Wang, Y., Li, C., Li, Y., Wang, Y., 2019. Neogene expansion of the qilian Shan, north Tibet: implications for the dynamic evolution of the Tibetan plateau. *Tectonics* 38 (3), 1018–1032. <https://doi.org/10.1029/2018tc005258>.
- Portner, R.A., Hendrix, M.S., Stalker, J.C., Miggins, D.P., Sheriff, S.D., Colpron, M., 2011. Sedimentary response to orogenic exhumation in the northern Rocky Mountain Basin and Range province, Flint Creek basin, west-central Montana. *Can. J. Earth Sci.* 48 (7), 1131–1154. <https://doi.org/10.1139/e10-107>.
- Pullen, A., Kapp, P., McCallister, A.T., Chang, H., Gehrels, G.E., Garzanti, C.N., Heermance, R.V., Ding, L., 2011. Qaidam Basin and northern Tibetan Plateau as dust sources for the Chinese Loess Plateau and paleoclimatic implications. *Geology* 39 (11), 1031–1034. <https://doi.org/10.1130/g32296.1>.
- Pundir, S., Adlakha, V., Devrani, R., Kumar, S., 2021. Tectonic control over shallow crustal exhumation across the India-asia convergent margin. *Tectonics* 40 (10). <https://doi.org/10.1029/2021tc006722>.
- Rahl, J.M., Reiners, P.W., Campbell, I.H., Nicolescu, S., Allen, C.M., 2003. Combined single-grain (U-Th)/He and U/Pb dating of detrital zircons from the Navajo Sandstone, Utah. *Geology* 31 (9), 761–764. <https://doi.org/10.1130/G19653.1>.
- Rahman, M.J.J., Faupl, P., 2003. 40Ar/39Ar multigrain dating of detrital white mica of sandstones of the Surma Group in the Sylhet Trough, Bengal Basin, Bangladesh. *Sediment. Geol.* 155 (3–4), 383–392. [https://doi.org/10.1016/S0037-0738\(02\)00188-4](https://doi.org/10.1016/S0037-0738(02)00188-4).
- Reiners, P.W., 2005. Zircon (U-Th)/He thermochronometry. *Rev. Mineral. Geochem.* 58 (1), 151–179. <https://doi.org/10.2138/rmg.2005.58.6>.
- Reiners, P.W., Farley, K.A., Hickey, H.J., 2002. He diffusion and (U-Th)/He thermochronometry of zircon: initial results from Fish Canyon Tuff and Gold Butte. *Tectonophysics* 349 (1–4), 297–308. [https://doi.org/10.1016/S0040-1951\(02\)00058-6](https://doi.org/10.1016/S0040-1951(02)00058-6).
- Reiners, P.W., Spell, T.L., Nicolescu, S., Zanetti, K.A., 2004. Zircon (U-Th)/He thermochronometry: He diffusion and comparisons with 40Ar/39Ar dating. *Geochem. Cosmochim. Acta* 68 (8), 1857–1887. <https://doi.org/10.1016/j.gca.2003.10.021>.
- Ren, X., Nie, J., Saylor, J.E., Li, H., Bush, M.A., Horton, B.K., 2019. Provenance control on chemical weathering index of fluvio-lacustrine sediments: evidence from the Qaidam Basin, NE Tibetan plateau. *G-cubed* 20 (7), 3216–3224. <https://doi.org/10.1029/2019gc008330>.
- Rieser, A.B., Liu, Y., Genser, J., Neubauer, F., Handler, R., Ge, X.-H., 2006a. Uniform Permian 40Ar/39Ar detrital mica ages in the eastern Qaidam Basin (NW China): where is the source? *Terra. Nova* 18 (1), 79–87. <https://doi.org/10.1111/j.1365-3121.2005.00666.x>.
- Rieser, A.B., Liu, Y., Genser, J., Neubauer, F., Handler, R., Friedl, G., Ge, X.-H., 2006b. 40Ar/39Ar ages of detrital white mica constrain the Cenozoic development of the intracontinental Qaidam Basin, China. *Geol. Soc. Am. Bull.* 118 (11–12), 1522–1534. <https://doi.org/10.1130/B25962.1>.
- Rieser, A.B., Neubauer, F., Liu, Y., Ge, X., 2005. Sandstone provenance of north-western sectors of the intracontinental Cenozoic Qaidam basin, western China: tectonic vs. climatic control. *Sediment. Geol.* 177 (1–2), 1–18. <https://doi.org/10.1016/j.sedgeo.2005.01.012>.
- Rieser, A.B., Neubauer, F., Liu, Y., Genser, J., 2010. Walking through geologic history across a Neogene, incised anticline of the northern margin of the Tibetan plateau: review and synthesis. *Austrian Journal of Earth Sciences* 103 (1).
- Rieser, A.B., Neubauer, F., Liu, Y., Genser, J., Handler, R., Ge, X.-H., Friedl, G., 2007. 40Ar/39Ar dating of detrital white mica as a complementary tool for provenance analysis: a case study from the cenozoic Qaidam Basin (China). In: *Sedimentary Processes, Environments and Basins*, pp. 301–325. <https://doi.org/10.1002/9781444304411.ch14>.
- Sang, H.Q., Wang, F., He, H.Y., Wang, Y.L., Yang, L.K., Zhu, R.X., 2006. Intercalibration of ZBH-25 biotite reference material utilized for K/Ar and 40Ar/39Ar age determination. *Acta Petrol. Sin.* 22 (12), 3059–3078 in Chinese with English abstract.
- Shen, X., Jian, X., Li, C., Liu, J.T., Chang, Y.-P., Zhang, S., Mei, H., Fu, H., Zhang, W., 2021. Submarine topography-related spatial variability of the southern Taiwan Strait sands (East Asia). *Mar. Geol.* 436 <https://doi.org/10.1016/j.margeo.2021.106495>.
- Shi, W., Wang, F., Yang, L., Wu, L., Zhang, W., 2018. Diachronous growth of the Altyn tagh mountains: constraints on propagation of the northern Tibetan margin from (U-Th)/He dating. *J. Geophys. Res. Solid Earth* 123 (7), 6000–6018. <https://doi.org/10.1029/2017jb014844>.
- Sobel, E.R., Arnaud, N., 1999. A possible middle Paleozoic suture in the Altyn Tagh, NW China. *Tectonics* 18 (1), 64–74. <https://doi.org/10.1029/1998TC900023>.

- Sobel, E.R., Strecker, M.R., 2003. Uplift, exhumation and precipitation: tectonic and climatic control of Late Cenozoic landscape evolution in the northern Sierras Pampeanas, Argentina. *Basin Res.* 15 (4), 431–451. <https://doi.org/10.1046/j.1365-2117.2003.00214.x>.
- Sobel, E.R., Arnaud, N., Jolivet, M., Ritts, B.D., Brunel, M., 2001. Jurassic to Cenozoic exhumation history of the Altyn Tagh range, northwest China, constrained by ⁴⁰Ar/³⁹Ar and apatite fission track thermochronology. In: *Paleozoic and Mesozoic Tectonic Evolution of Central and Eastern Asia: from Continental Assembly to Intracontinental Deformation*. <https://doi.org/10.1130/0-8137-1194-0.247>.
- Song, S., Zhang, L., Niu, Y., Su, L., Jian, P., Liu, D., 2005. Geochronology of diamond-bearing zircons from garnet peridotite in the North Qaidam UHPM belt, Northern Tibetan Plateau: a record of complex histories from oceanic lithosphere subduction to continental collision. *Earth Planet. Sci. Lett.* 234 (1–2), 99–118. <https://doi.org/10.1016/j.epsl.2005.02.036>.
- Spiegel, C., Siebel, W., Kuhlemann, J., Frisch, W., 2004. Toward a comprehensive provenance analysis: a multi-method approach and its implications for the evolution of the Central Alps. In: *Detrital Thermochronology - Provenance Analysis, Exhumation, and Landscape Evolution of Mountain Belts*. <https://doi.org/10.1130/0-8137-2378-7.37>.
- Staisch, L.M., Niemi, N.A., Clark, M.K., Chang, H., 2020. The Cenozoic evolution of crustal shortening and left-lateral shear in the central East Kunlun Shan: implications for the uplift history of the Tibetan plateau. *Tectonics* 39 (9). <https://doi.org/10.1029/2020tc006065>.
- Stickroth, S.F., Carrapa, B., DeCelles, P.G., Gehrels, G.E., Thomson, S.N., 2019. Tracking the growth of the Himalayan fold-and-thrust belt from lower Miocene foreland basin strata: dumri formation, western Nepal. *Tectonics* 38 (11), 3765–3793. <https://doi.org/10.1029/2018tc005390>.
- Stockli, D.F., Najman, Y.M.R., 2020. Earth's dynamic past revealed by detrital thermochronometry. *Elements* 16 (5), 311–317. <https://doi.org/10.2138/gselements.16.5.311>.
- Stuart, F., 2002. The exhumation history of orogenic belts from ⁴⁰Ar/³⁹Ar ages of detrital micas. *Mineral. Mag.* 66 (1), 121–135. <https://doi.org/10.1180/0026461026610017>.
- Sun, G., Wang, M., Guo, J., Wang, Y., Yang, Y., 2020b. Geochemical significance of clay minerals and elements in Paleogene sandstones in the center of the northern margin of the Qaidam Basin, China. *Minerals* 10 (6), 505. <https://www.mdpi.com/2075-163X/10/6/505>.
- Sun, G., Wang, Y., Jiang, Y., Pan, S., Zhang, S., Zhang, M., 2020a. Provenance and tectonic setting of Paleogene sandstone in the center of the northern Qaidam Basin, China. *Journal of Natural Gas Geoscience* 5 (5), 273–284. <https://doi.org/10.1016/j.jnggs.2020.09.002>.
- Sun, J., 2002. Provenance of loess material and formation of loess deposits on the Chinese Loess Plateau. *Earth Planet. Sci. Lett.* 203 (3), 845–859. [https://doi.org/10.1016/S0012-821X\(02\)00921-4](https://doi.org/10.1016/S0012-821X(02)00921-4).
- Sun, J.-F., Yang, J.-H., Wu, F.-Y., Li, X.-H., Yang, Y.-H., Xie, L.-W., Wilde, S.A., 2010. Magma mixing controlling the origin of the Early Cretaceous Fangshan granitic pluton, North China Craton: in situ U–Pb age and Sr, Nd, Hf-and O-isotope evidence. *Lithos* 120 (3–4), 421–438. <https://doi.org/10.1016/j.lithos.2010.09.002>.
- Sun, X., Kuiper, K.F., Tian, Y., Li, C.a., Zhang, Z., Gemignani, L., Guo, R., de Breijl, V.H.L., Wijbrans, J.R., 2020. ⁴⁰Ar/³⁹Ar mica dating of late Cenozoic sediments in SE Tibet: implications for sediment recycling and drainage evolution. *J. Geol. Soc.* 177 (4), 843–854. <https://doi.org/10.1144/jgs2019-099>. Article.
- Sun, X., Li, C.a., Kuiper, K.F., Wang, J., Tian, Y., Vermeesch, P., Zhang, Z., Zhao, J., Wijbrans, J.R., 2018. Geochronology of detrital muscovite and zircon constrains the sediment provenance changes in the Yangtze River during the late Cenozoic [Article]. *Basin Res.* 30 (4), 636–649. <https://doi.org/10.1111/bre.12268>.
- Sun, X., Li, C.a., Kuiper, K.F., Zhang, Z., Gao, J., Wijbrans, J.R., 2016. Human impact on erosion patterns and sediment transport in the Yangtze River. *Global Planet. Change* 143, 88–99. <https://doi.org/10.1016/j.gloplacha.2016.06.004>.
- Sun, X., Tian, Y., Kuiper, K.F., Li, C.a., Zhang, Z., Wijbrans, J.R., 2021. No yangtze river prior to the late miocene: evidence from detrital muscovite and K-feldspar ⁴⁰Ar/³⁹Ar geochronology. *Geophys. Res. Lett.* 48 (5) <https://doi.org/10.1029/2020gl089903>.
- Sun, Y., Ouyang, Q., Lang, X., Pang, K., Wu, C., Chen, Z., Zhou, C., 2023. Global sea-level fall triggered Ediacaran–Cambrian unconformity in North China craton. *Earth Planet. Sci. Lett.* 622 <https://doi.org/10.1016/j.epsl.2023.118411>.
- Szulc, A.G., Najman, Y., Sinclair, H.D., Pringle, M., Bickle, M., Chapman, H., Garzanti, E., Andò, S., Huyghe, P., Mugnier, J.L., Ojha, T., DeCelles, P., 2006. Tectonic evolution of the Himalaya constrained by detrital ⁴⁰Ar–³⁹Ar, Sm–Nd and petrographic data from the Siwalik foreland basin succession, SW Nepal. *Basin Res.* 18 (4), 375–391. <https://doi.org/10.1111/j.1365-2117.2006.00307.x>.
- Thiede, R.C., Bookhagen, B., Arrowsmith, J.R., Sobel, E.R., Strecker, M.R., 2004. Climatic control on rapid exhumation along the southern Himalayan front. *Earth Planet. Sci. Lett.* 222 (3–4), 791–806. <https://doi.org/10.1016/j.epsl.2004.03.015>.
- Tian, P., Yuan, W., Yang, X., Feng, Z., Chen, X., Yuan, E., 2020. Multi-stage tectonic events of the Eastern Kunlun Mountains, Northern Tibetan Plateau constrained by fission track thermochronology. *J. Asian Earth Sci.* 198 <https://doi.org/10.1016/j.jseas.2020.104428>.
- Tong, K., Li, Z., Zhu, L., Tao, G., Zhang, Y., Yang, W., Zhang, J., 2020. Fold-and-thrust deformation of the hinterland of Qilian Shan, northeastern Tibetan Plateau since Mesozoic with implications for the plateau growth. *J. Asian Earth Sci.* 198 <https://doi.org/10.1016/j.jseas.2019.104131>.
- Tshering, P., 2007. *Detrital Muscovite Thermochronology in Two Drainage Basins in Western Bhutan* (Doctoral Dissertation). Massachusetts Institute of Technology.
- Uddin, A., Hames, W.E., Zahid, K.M., 2010. Laser ⁴⁰Ar/³⁹Ar age constraints on Miocene sequences from the Bengal basin: implications for middle Miocene denudation of the eastern Himalayas. *J. Geophys. Res. Solid Earth* 115, B07416. <https://doi.org/10.1029/2009jb006401>. Article.
- Van Hoang, L., Clift, P.D., Mark, D., Zheng, H., Tan, M.T., 2010. Ar–Ar muscovite dating as a constraint on sediment provenance and erosion processes in the Red and Yangtze River systems, SE Asia. *Earth Planet. Sci. Lett.* 295 (3–4), 379–389. <https://doi.org/10.1016/j.epsl.2010.04.012>.
- Vermeesch, P., Resentini, A., Garzanti, E., 2016. An R package for statistical provenance analysis. *Sediment. Geol.* 336, 14–25. <https://doi.org/10.1016/j.sedgeo.2016.01.009>.
- von Eynatten, H., Dunkl, I., 2012. Assessing the sediment factory: the role of single grain analysis. *Earth Sci. Rev.* 115 (1–2), 97–120. <https://doi.org/10.1016/j.earscirev.2012.08.001>.
- von Eynatten, H., Wijbrans, J., 2003. Precise tracing of exhumation and provenance using ⁴⁰Ar/³⁹Ar geochronology of detrital white mica: the example of the Central Alps. *Geological Society, London, Special Publications* 208 (1), 289–305. <https://doi.org/10.1144/GSL.SP.2003.208.01.14>.
- von Eynatten, H., Schlunegger, F., Gaupp, R., Wijbrans, J.R., 1999. Exhumation of the Central Alps: evidence from ⁴⁰Ar/³⁹Ar laserprobe dating of detrital white micas from the Swiss Molasse Basin. *Terra. Nova* 11 (6), 284–289. <https://doi.org/10.1046/j.1365-3121.1999.00260.x>.
- Wang, F., Ching-hua, L., Li, Q., Wan, J., Zheng, D., Wang, E., 2002. Unroofing around Qaidam Basin of northern Tibet at 30 Ma: constraints from ⁴⁰Ar/³⁹Ar and FT thermochronology on granitoids. *Sci. China, Ser. B: Chem.* 45, 70–83. <https://doi.org/10.1007/BF02932209>.
- Wang, L., Jian, X., Fu, H., Zhang, W., Shang, F., Fu, L., 2023. Decoupled local climate and chemical weathering intensity of fine-grained siliciclastic sediments from a paleomegalake: an example from the Qaidam basin, northern Tibetan Plateau. *Sediment. Geol.* 454 <https://doi.org/10.1016/j.sedgeo.2023.106462>.
- Wang, L., MacLennan, S.A., Cheng, F., 2020. From a proximal-deposition-dominated basin sink to a significant sediment source to the Chinese Loess Plateau: insight from the quantitative provenance analysis on the Cenozoic sediments in the Qaidam basin, northern Tibetan Plateau. *Palaeogeogr. Palaeoclimatol. Palaeoecol.* 556, 109883 <https://doi.org/10.1016/j.palaeo.2020.109883>.
- Wang, Q., 2023. *Cenozoic Basin Mountain Coupling in Western Qaidam Basin: Thermal Chronology Constraints from Detrital Mica ⁴⁰Ar–³⁹Ar and Apatite Fission Track Dating* (Master's Thesis). Jilin University. <https://link.cnki.net/doi/10.27162/d.cnki.gjlin.2023.001852>.
- Wang, W., Zhang, P., Duan, L., Zhang, B., Liu, K., Huang, R., Liu, C., Zhang, Z., Zheng, D., Zheng, W., Zhang, H., 2022b. Cenozoic stratigraphic chronology and sedimentary-tectonic evolution of the Qaidam Basin. *Chin. Sci. Bull.* 67 (28–29), 3452–3475. <https://doi.org/10.1360/tb-2022-0108>.
- Wang, W., Zhang, P., Garzanti, C.N., Liu, C., Zhang, Z., Pang, J., Wang, Y., Zheng, D., Zheng, W., Zhang, H., 2022a. Pulsed rise and growth of the Tibetan Plateau to its northern margin since ca. 30 Ma. *Proc Natl Acad Sci U S A* 119 (8). <https://doi.org/10.1073/pnas.2120364119>.
- Wang, W., Zheng, W., Zhang, P., Li, Q., Kirby, E., Yuan, D., Zheng, D., Liu, C., Wang, Z., Zhang, H., Pang, J., 2017. Expansion of the Tibetan plateau during the neogene. *Nat. Commun.* 8, 15887 <https://doi.org/10.1038/ncomms15887>.
- Wang, Y., Zhang, X., Wang, E., Zhang, J., Li, Q., Sun, G., 2005. ⁴⁰Ar/³⁹Ar thermochronological evidence for formation and Mesozoic evolution of the northern-central segment of the Altyn Tagh fault system in the northern Tibetan Plateau. *Geol. Soc. Am. Bull.* 117 (9–10), 1336–1346. <https://doi.org/10.1130/B25685.1>.
- Wang, Y., Zheng, J., Zheng, Y., 2018. Mesozoic–Cenozoic exhumation history of the Qimen Tagh Range, northeastern margins of the Tibetan Plateau: evidence from apatite fission track analysis. *Gondwana Res.* 58, 16–26. <https://doi.org/10.1016/j.gr.2018.01.014>.
- White, N.M., Pringle, M., Garzanti, E., Bickle, M., Najman, Y., Chapman, H., Friend, P., 2002. Constraints on the exhumation and erosion of the High Himalayan Slab, NW India, from foreland basin deposits. *Earth Planet. Sci. Lett.* 195 (1–2), 29–44. [https://doi.org/10.1016/S0012-821X\(01\)00565-9](https://doi.org/10.1016/S0012-821X(01)00565-9).
- Wobus, C.W., Hodges, K.V., Whipple, K.X., 2003. Has focused denudation sustained active thrusting at the Himalayan topographic front? *Geology* 31 (10), 861–864. <https://doi.org/10.1130/G19730.1>.
- Wobus, C.W., Whipple, K.X., Hodges, K.V., 2006. Neotectonics of the central Nepalese Himalaya: constraints from geomorphology, detrital ⁴⁰Ar/³⁹Ar thermochronology, and thermal modeling. *Tectonics* 25 (4). <https://doi.org/10.1029/2005tc001935/n/a-n/a>.
- Wu, C., Zuzza, A.V., Chen, X., Ding, L., Levy, D.A., Liu, C., Liu, W., Jiang, T., Stockli, D.F., 2019a. Tectonics of the eastern Kunlun range: Cenozoic reactivation of a paleozoic-early Mesozoic orogen. *Tectonics* 38 (5), 1609–1650. <https://doi.org/10.1029/2018tc005370>.
- Wu, C., Zuzza, A.V., Zhou, Z., Yin, A., McRivette, M.W., Chen, X., Ding, L., Geng, J., 2019b. Mesozoic–Cenozoic evolution of the Eastern Kunlun Range, central Tibet, and implications for basin evolution during the Indo-Asian collision. *Lithosphere* 11 (4), 524–550. <https://doi.org/10.1130/L1065.1>.
- Wu, L., Xiao, A., Wang, L., Mao, L., Wang, L., Dong, Y., Xu, B., 2012a. EW-trending uplifts along the southern side of the central segment of the Altyn Tagh Fault, NW China: insight into the rising mechanism of the Altyn Mountain during the Cenozoic. *Sci. China Earth Sci.* 55 (6), 926–939. <https://doi.org/10.1007/s11430-012-4402-7>.
- Wu, L., Xiao, A., Yang, S., Wang, L., Mao, L., Wang, L., Dong, Y., Xu, B., 2012b. Two-stage evolution of the Altyn Tagh Fault during the Cenozoic: new insight from provenance analysis of a geological section in NW Qaidam Basin, NW China. *Terra. Nova* 24 (5), 387–395. <https://doi.org/10.1111/j.1365-3121.2012.01077.x>.
- Xia, G., Wu, C., Li, G., Li, G., Yi, H., Wagerich, M., 2020. Cenozoic growth of the eastern Kunlun range (northern Tibetan plateau): evidence from sedimentary records in the

- southwest Qaidam Basin. *Int. Geol. Rev.* 63 (6), 769–786. <https://doi.org/10.1080/00206814.2020.1731717>.
- Xing, Y., Song, B., Li, T., Li, S., Yan, K., Wang, Q., Zhang, H., Wan, X., 2023. Eocene to miocene charophytes from the Qaidam Basin on the northern Tibetan Plateau and its calibration to the geomagnetic polarity time scale. *Rev. Palaeobot. Palynol.* 308 <https://doi.org/10.1016/j.revpalbo.2022.104784>.
- Xu, J., Stockli, D.F., Snedden, J.W., 2017. Enhanced provenance interpretation using combined U–Pb and (U–Th)/He double dating of detrital zircon grains from lower Miocene strata, proximal Gulf of Mexico Basin, North America. *Earth Planet Sci. Lett.* 475, 44–57. <https://doi.org/10.1016/j.epsl.2017.07.024>.
- Xu, Q.-Q., Ji, J.-Q., Zhao, L., Gong, J.-F., Zhou, J., He, G.-Q., Zhong, D.-L., Wang, J.-D., Griffiths, L., 2013. Tectonic evolution and continental crust growth of Northern Xinjiang in northwestern China: remnant ocean model. *Earth Sci. Rev.* 126, 178–205. <https://doi.org/10.1016/j.earscirev.2013.08.005>.
- Xu, Z., Li, H., Chen, W., Wu, C., Yang, J., Jin, X., Chen, F., 2002. A large ductile sinistral strike-slip shear zone and its movement timing in the south qilian mountains, western China. *Acta Geologica Sinica-English Edition* 76 (2), 183–193. <https://doi.org/10.1111/j.1755-6724.2002.tb00084.x>.
- Yan, Z., Yang, R., Yang, Y., Liu, Y., Galy, A., Fang, X., 2024. Late Miocene drainage reorganization on the NE Tibetan Plateau linked to growth of the Qilian Shan revealed by coupled carbonate Sr-silicate Nd isotopic tracers. *Palaeogeogr. Palaeoclimatol. Palaeoecol.* 638, 112038 <https://doi.org/10.1016/j.palaeo.2024.112038>.
- Yang, Y., Fang, X., Galy, A., Jin, Z., Wu, F., Yang, R., Zhang, W., Zan, J., Liu, X., Gao, S., 2016. Plateau uplift forcing climate change around 8.6 Ma on the northeastern Tibetan Plateau: evidence from an integrated sedimentary Sr record. *Palaeogeogr. Palaeoclimatol. Palaeoecol.* 461, 418–431. <https://doi.org/10.1016/j.palaeo.2016.09.002>.
- Yang, Y., Galy, A., Yang, R., Liu, Y., Zhang, W., Ruan, X., Fang, X., Jin, Z., Song, B., Yan, M., Zhang, G., Cao, K., Shen, T., Mao, Z., Wu, F., Zhang, F., 2022. Intense Metamorphism-Generated Radiogenic Sr Regulated Cenozoic Water Sr Isotope Evolution on the NE Tibetan Plateau: A Perspective on Qilian Orogen Denudation and Asian Eolian Transport. *GSA Bulletin Geological Society of America Bulletin*. <https://doi.org/10.1130/b36525.1>.
- Yi, K., Cheng, F., Jolivet, M., Li, J., Guo, Z., 2024. Carbonate U-Pb ages constrain Paleocene motion along the Altyn Tagh fault in response to the India-asia collision. *Geophys. Res. Lett.* 51 (8), e2023GL107716 <https://doi.org/10.1029/2023GL107716>.
- Yin, A., Dang, Y.Q., Zhang, M., Chen, X.H., McRivette, M.W., 2008. Cenozoic tectonic evolution of the Qaidam basin and its surrounding regions (Part 3): structural geology, sedimentation, and regional tectonic reconstruction. *Geol. Soc. Am. Bull.* 120 (7–8), 847–876. <https://doi.org/10.1130/b26232.1>.
- Yin, A., Rumelhart, P., Butler, R., Cowgill, E., Harrison, T., Foster, D., Ingersoll, R., Qing, Z., Xian-Qiang, Z., Xiao-Feng, W., 2002. Tectonic history of the Altyn Tagh fault system in northern Tibet inferred from Cenozoic sedimentation. *Geol. Soc. Am. Bull.* 114 (10), 1257–1295. [https://doi.org/10.1130/0016-7606\(2002\)114<1257:THOTAT>2.0.CO;2](https://doi.org/10.1130/0016-7606(2002)114<1257:THOTAT>2.0.CO;2).
- Yin, J., Zhang, S., Wu, Z., 2020. Provenance analysis of the Paleogene strata in the northern Qaidam Basin, China: evidences from sediment distribution, heavy mineral assemblages and detrital zircon U–Pb geochronology. *Minerals* 10 (10). <https://doi.org/10.3390/min10100854>.
- Yuan, W., Dong, J., Shicheng, W., Carter, A., 2006. Apatite fission track evidence for neogene uplift in the eastern Kunlun mountains, northern qinghai–tibet plateau, China. *J. Asian Earth Sci.* 27 (6), 847–856. <https://doi.org/10.1016/j.jseas.2005.09.002>.
- Zaun, P., Wagner, G., 1985. Fission-track stability in zircons under geological conditions. *Nucl. Tracks Radiat. Meas.* 10 (3), 303–307, 1982.
- Zhang, J., Meng, F., Yu, S., Chen, W., Chen, S., 2007. 39Ar–40Ar geochronology of high-pressure/low-temperature blueschist and eclogite in the North Altyn Tagh and their tectonic implications. *Chin. Geol.* 34 (4), 558–564 in Chinese with English abstract.
- Zhang, S., Jian, X., Pullen, A., Fu, L., Liang, H., Hong, D., Zhang, W., 2020. Tectonomagmatic events of the Qilian orogenic belt in northern Tibet: new insights from detrital zircon geochronology of river sands. *Int. Geol. Rev.* 63 (8), 917–940. <https://doi.org/10.1080/00206814.2020.1734876>.
- Zhang, W., Jian, X., Fu, L., Feng, F., Guan, P., 2018. Reservoir characterization and hydrocarbon accumulation in late Cenozoic lacustrine mixed carbonate-siliciclastic fine-grained deposits of the northwestern Qaidam basin, NW China. *Mar. Petrol. Geol.* 98, 675–686. <https://doi.org/10.1016/j.marpetgeo.2018.09.008>.
- Zheng, Z., Chen, Y., Deng, X., Yue, S., Chen, H., 2016. Muscovite 40Ar/39Ar dating of the baiguanhu W–Sn orefield, qimantag, East Kunlun mountains, and its geological implications. *Chin. Geol.* 43 (4), 1341–1352 in Chinese with English abstract.
- Zhou, B., Dong, Y., Yang, Z., Genser, J., Neubauer, F., He, D., Hui, B., Shi, X., 2022. Detrital U–Pb zircon and 40Ar/39Ar muscovite geochronology of Triassic and Jurassic strata in the southern East Kunlun, northern Tibet Plateau and their geological implications. *Geol. J.* <https://doi.org/10.1002/gj.4569>.
- Zhou, H., Chen, L., Diwu, C., Lei, C., Li, S., 2018. Cenozoic uplift of the qimantag mountains, northeastern Tibet: constraints from provenance analysis of cenozoic sediments in Qaidam Basin. *Geol. J.* 53 (6), 2613–2632. <https://doi.org/10.1002/gj.3095>.
- Zhou, J., Ji, J.Q., Han, B.F., Gong, J.F., Xu, Q.Q., Guo, Z.J., 2008. 40Ar/39Ar geochronology of mafic dykes in north Xinjiang. *Acta Petrol. Sin.* 24 (5), 997–1010 in Chinese with English abstract.
- Zhu, W., Wu, C., Wang, J., Zhou, T., 2019. Provenance analysis of detrital monazite, zircon and Cr-spinel in the northern Tibetan plateau: implications for the paleozoic tectonothermal history of the Altyn tagh and qimen tagh ranges. *Basin Res.* 31 (3), 539–561. <https://doi.org/10.1111/bre.12333>.
- Zhu, W., Wu, C., Wang, J., Zhou, T., Li, J., Zhang, C., Li, L., 2017. Heavy mineral compositions and zircon U–Pb ages of Cenozoic sandstones in the SW Qaidam basin, northern Tibetan Plateau: implications for provenance and tectonic setting. *J. Asian Earth Sci.* 146, 233–250. <https://doi.org/10.1016/j.jseas.2017.05.023>.
- Zhuang, G., Hourigan, J.K., Ritts, B.D., Kent-Corson, M.L., 2011. Cenozoic multiple-phase tectonic evolution of the northern Tibetan Plateau: constraints from sedimentary records from Qaidam basin, Hexi Corridor, and Subei basin, northwest China. *Am. J. Sci.* 311 (2), 116–152. <https://doi.org/10.2475/02.2011.02>.
- Zhuang, G., Najman, Y., Tian, Y., Carter, A., Gemignani, L., Wijbrans, J., Jan, M.Q., Khan, M.A., 2018. Insights into the evolution of the Hindu Kush–Kohistan–Karakoram from modern river sand detrital geo- and thermochronological studies. *J. Geol. Soc.* 175 (6), 934–948. <https://doi.org/10.1144/jgs2018-007>.
- Zhuang, G., Zhang, Y.G., Hourigan, J., Ritts, B., Hren, M., Hou, M., Wu, M., Kim, B., 2019. Microbial and geochronologic constraints on the neogene paleotopography of northern Tibetan plateau. *Geophys. Res. Lett.* 46 (3), 1312–1319. <https://doi.org/10.1029/2018gl081505>.
- Zuza, A.V., Wu, C., Reith, R.C., Yin, A., Li, J., Zhang, J., Zhang, Y., Wu, L., Liu, W., 2018. Tectonic evolution of the Qilian Shan: an early Paleozoic orogen reactivated in the Cenozoic. *GSA Bulletin Geological Society of America Bulletin* 130 (5–6), 881–925.